

Modeling Tube Clearance and Bounding the Effect of Friction in Concentric Tube Robot Kinematics

Junhyoung Ha[✉], Georgios Fagogenis, and Pierre E. Dupont[✉], *Fellow, IEEE*

Abstract—The shape of a concentric tube robot depends not only on the relative rotations and translations of its constituent tubes, but also on the history of relative tube displacements. Existing mechanics-based models neglect all history-dependent phenomena with the result that when calibrated on experimental data collected over a robot’s workspace, the maximum tip position error can exceed 8 mm for a 200-mm-long robot. In this paper, we develop a model that computes the bounding kinematic solutions in which Coulomb friction is acting either to maximize or minimize the relative twisting between each pair of contacting tubes. The path histories associated with these limiting cases correspond to first performing all tube translations and then performing relative tube rotations of sufficient angle so that the maximum Coulomb friction force is obtained along the interface of each contacting tube pair. The robot tip configurations produced by these path histories are shown experimentally to bound position error with respect to the estimated frictionless model compared to path histories comprised of translation or mixed translation and rotation. Intertube friction forces and torques are computed as proportional to the intertube contact forces. To compute these contact forces, the standard zero-clearance assumption that constrains the concentrically combined tubes to possess the same centerline is relaxed. The effects of clearance and friction are explored through numerical and physical experiments and it is shown that friction can explain much of the prediction error observed in existing models. This model is not intended for real-time control, but rather for path planning—to provide error bounds and to inform how the ordering of tube rotations and translations can be used to reduce the effect of friction.

Index Terms—Concentric tube robots, friction, model calibration, tube clearance.

NOMENCLATURE

n	Number of tubes.	$\mathbf{p}_i(s)$	Three-dimensional (3-D) centerline curve of tube i .
i	Tube index, numbered from outer to inner.	$\mathbf{R}_i(s)$	3×3 rotation matrix of body frame of tube i .
j	Arc-length discretization index, numbered from base to tip.	$\hat{\mathbf{e}}_z$	Unit z -axis vector, i.e., $[0 \ 0 \ 1]^T$.
k	Index renumbered from combined index ij .	$\mathbf{u}_i(s)$	3-D curvature vector of tube i .
s	Arc-length parameter.	$\hat{\mathbf{u}}_i(s)$	3-D pre-curvature vector of tube i .
		$\theta_{i,b}, \theta_b$	Base rotation of tube i and base rotation vector.
		$l_{i,b}, \mathbf{l}_b$	Translation of tube i and translation vector.
		$k_{i,xy}, k_{i,z}$	Bending and torsional stiffnesses of tube i .
		\mathbf{K}_i	3×3 stiffness matrix of tube i .
		$\mathbf{R}_z(\alpha)$	3×3 rotation matrix of rotation of α about z -axis.
		$g_i(s)$	Elastic potential energy per length of tube i .
		$\vec{\mathbf{u}}_i$	Vector comprised of discretized $\mathbf{u}_i(s)$.
		$\vec{\mathbf{u}}_i^*$	Vector comprised of discretized $\hat{\mathbf{u}}_i(s)$.
		$\vec{\mathbf{p}}_i$	Vector comprised of discretized $\mathbf{p}_i(s)$.
		$\vec{\mathbf{u}}$	Vector comprised of $\vec{\mathbf{u}}_i$ of all tubes.
		$\vec{\mathbf{u}}^*$	Vector comprised of $\vec{\mathbf{u}}_i^*$ of all tubes.
		$\vec{\mathbf{p}}$	Vector comprised of $\vec{\mathbf{p}}_i$ of all tubes.
		N_i	Number of discretized points on tube i .
		N	Sum of N_i of all tubes.
		$F(\vec{\mathbf{u}})$	Function that returns tube centerlines $\vec{\mathbf{p}}$ given tube curvatures $\vec{\mathbf{u}}$.
		$G(\vec{\mathbf{u}})$	Tube-contact constraint function.
		E	Potential energy of all tubes.
		\mathbf{K}	Matrix comprised of stiffnesses corresponding to $\vec{\mathbf{u}}$.
		ν	Poisson’s ratio.
		$\vec{\mathbf{u}}^*$	Nominal value of $\vec{\mathbf{u}}$ for linearization of $F(\vec{\mathbf{u}})$ and $G(\vec{\mathbf{u}})$.
		$\vec{\mathbf{p}}^*$	Value of $\vec{\mathbf{p}}$ corresponding to $\vec{\mathbf{u}}^*$.
		$\Delta\vec{\mathbf{u}}$	Difference between $\vec{\mathbf{u}}^*$ and $\vec{\mathbf{u}}$, i.e., $\vec{\mathbf{u}} - \vec{\mathbf{u}}^*$.
		$\Delta\vec{\mathbf{p}}$	Difference between $\vec{\mathbf{p}}^*$ and $\vec{\mathbf{p}}$, i.e., $\vec{\mathbf{p}} - \vec{\mathbf{p}}^*$.
		\mathbf{P}_{ij}	3×3 projection matrix of cross section of tube i at j -th discretized point.
		\mathbf{J}_p	Jacobian matrix of $F(\vec{\mathbf{u}})$.
		\mathbf{J}_ω	Jacobian matrix of $R_i(s)$ w.r.t. $\vec{\mathbf{u}}$.
		\mathbf{S}_{ij}	Selection matrix to pick $\mathbf{p}_i(s_{ij})$ and $-\mathbf{p}_{i+1}(s_{ij})$ from $\vec{\mathbf{p}}$.
		c_i	Clearance between tube i and tube $i + 1$.
		$r_{i,in}, r_{i,out}$	Inner and outer radii of tube i .
		$\mathbf{g}, \mathbf{X}_k, \mathbf{x}_k, q_k$	Initialization variables of inner loops of clearance model and friction model.
		\mathbf{Y}_k	Initialization variable of inner loop of friction model.

Manuscript received May 3, 2018; revised August 7, 2018; accepted October 7, 2018. This paper was recommended for publication by Associate Editor Kai Xu and Editor I-Ming Chen upon evaluation of the reviewers’ comments. This work was supported by the National Institutes of Health under Grant R01HL124020. (*Corresponding author: Pierre E. Dupont*)

The authors are with the Department of Cardiovascular Surgery, Boston Children’s Hospital, Harvard Medical School, Boston, MA 02115 USA (e-mail: hjhdog1@gmail.com; georgios.fagogenis@gmail.com; Pierre.Dupont@childrens.harvard.edu).

Color versions of one or more of the figures in this paper are available online at <http://ieeexplore.ieee.org>.

Digital Object Identifier 10.1109/TRO.2018.2878906

λ	Lagrange multiplier vector associated with tube contact constraint.
$Q(\lambda), h(\lambda)$	Variables computed in each iteration of inner loops of clearance model and friction model.
$f_{\text{normal},k}$	Normal contact force on outer tube applied by inner tube at $s_k (= s_{kj})$.
f_{normal}	Vector comprised of $f_{\text{normal},k}$ for all k .
$f_{\text{friction},k}$	Friction force on outer tube applied by inner tube at $s_k (= s_{kj})$.
$\tau_{i,k}$	Torque on tube i induced by tube-to-tube friction at $s_k (= s_{kj})$.
τ	Vector comprised of $\tau_{i,k}$ for all k .
μ_k	Friction coefficient between tubes associated with k -th contact constraint.
η_k	Direction of prior rotation of inner tube w.r.t. outer tube at k -th contact constraint. Either 1 (CCW) or -1 (CW).

I. INTRODUCTION

CONCENTRIC tube robots are being applied to many types of medical interventions including surgery inside the heart [1]–[4], the brain [5], [6], and the lungs [7]–[9]. Many of these implementations have employed a mechanics-based kinematic model derived from the Cosserat rod model [10], [11] or a potential energy formulation [12], [13]. While the resulting kinematic model is more complex than standard robot models, real-time implementations have been successfully demonstrated [5]. The model does neglect some physical phenomena, however, resulting in larger kinematic model errors than is desirable for medical applications. For example, the reported mean and maximum tip position errors were 4.2 and 8.3 mm for a 207-mm-long robot [10] and 2.89 and 8.49 mm for a 200-mm-long robot [11]. Since targeting errors of 1–2 mm can be significant in surgeries performed near critical structures, these are large modeling errors. To compensate, image-based feedback is often needed, necessitating a higher skill level on the part of the operator.

A particular shortcoming of current models is that they do not include the effect of path history on robot shape, as shown in Fig. 1. To investigate how much of the unmodeled behavior may be due to friction, this paper formulates a mechanics-based model of tube-on-tube Coulomb friction by deriving expressions for the distributed contact forces between the tubes. The goal of this paper is develop bounds on the effect of friction on the kinematic solution. Such a model can be used in path planning and can motivate potential future work incorporating path history in real-time control. To reduce model complexity, a number of simplifications are made as described in the paragraphs below.

Small nonzero clearances between tubes: The frictionless model assumes that all overlapping tubes conform to a single centerline curve, which implies that there is no clearance between tubes. In reality, however, a finite clearance must be used, i.e., a small gap must exist between the outer diameter of the inner tube and the inner diameter of the outer tube. If this clearance is too small, the tubes bind up and cannot be rotated and translated. It is necessary to include clearance in the model in order to compute the distribution and magnitude of the intertube contact forces. Prior work on friction modeling did not

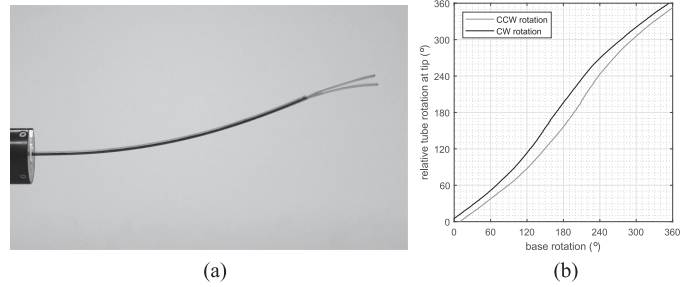


Fig. 1. Path dependence of concentric tube pair. (a) Superimposed photographs of robot shapes achieved by clockwise and counterclockwise rotation for a base angle of 120°. (b) Relative tube rotation angle at tip versus base.

include intertube clearance and consequently only provided an approximate solution [14]. As formulated in this paper, however, clearances are assumed to be small (empirically, up to 2% of the minimum radius of tube curvature is acceptable).

Coulomb friction is assumed: We assume that torsional and translational friction between the tubes is purely due to Coulomb friction. The Coulomb friction force F_C for unidirectional sliding at velocity v is given by [15]

$$F_C = \begin{cases} -\mu F_N, & v > 0 \\ \mu F_N, & v < 0 \\ -\mu F_N < F_C < \mu F_N, & v = 0 \end{cases} \quad (1)$$

in which F_N is the normal force of contact and μ is the friction coefficient. This model assumes that at zero velocity (i.e., the case considered in this paper), friction produces the minimum force sufficient to resist motion up to the limit of $\pm\mu F_N$. For tube-on-tube friction, the clearance model is used to compute the normal contact force.

Only tube twisting due to friction is modeled: We neglect any effect of friction through relative tube translation on tube bending, longitudinal compression, and tube buckling. Neglect of bending is justified based on experimental observation as shown in Section V-B. Longitudinal rigidity is an assumption of the frictionless model.

We solve for limiting solutions in which Coulomb friction either maximizes or minimizes the relative twist between contacting tube pairs: An actual robot path is comprised of tube rotations and translations that can vary in direction and magnitude. For these arbitrary path histories, the intertube friction force acting at any particular arc length along a tube pair may lie “inside the friction cone” since Coulomb friction generates the minimum force necessary to prevent motion. In the most general case, one would need to model the propagation of slip with arc length as pairs of tubes are rotated. Furthermore, even if tubes are considered longitudinally rigid, tube translation will reduce frictional torsion since a component of the friction force will be directed longitudinally. To reduce overall modeling complexity, these effects are neglected.

The contribution of this paper is to derive a model that provides estimates of the maximum error introduced by friction at any point in joint space. The model assumes that a configuration in joint space is reached by first translating all tubes and then performing relative tube rotations of sufficient magnitude prior

to reaching the goal configuration that the maximum Coulomb torque is applied along the entire arc length of each contacting tube pair. This approach provides a set of solutions corresponding to positive and negative rotations for each contacting tube pair. We show experimentally that these solutions provide estimates of the maximum error introduced by friction.

The model is derived using a convex optimization approach that solves for intertube contact and friction forces by considering the clearance between tubes. Additional assumptions used are that tube cross sections are circular and no external forces are applied. The formulation for the intertube contact minimizes elastic potential energy while allowing each tube's centerline curve to vary within the clearances of its inner and outer neighbors. This paper extends the results of [16] by incorporating friction forces and torques in the derivations and numerical experiments and by reporting physical experiments supporting the clearance and friction models. In addition, this paper provides more rigorous mathematical formulations compared to [16] of the Jacobian matrices that transform curvature changes to centerlines changes and body frame rotations.

While not related to concentric tube robots, there is a literature on friction modeling that considers some of the same issues. For example, the mechanisms literature considers the modeling of joints with clearance and friction [17]. In the robotic steering of needles through soft tissue, friction between the needle and tissue can generate torsional twisting of the needle [18]. In the analysis of tendon-driven continuum robots, the modeling of tendon friction has received considerable attention [19]–[22].

The paper is organized as follows. The kinematics in the presence of tube clearances are derived in Section II as an optimization problem. The following section introduces Coulomb friction into the model. Section IV presents a set of numerical experiments to investigate the effect of the clearance and friction on robot shape and intertube contact forces. Next, a set of physical experiments validating the tube clearance and the friction models are described. Conclusions are presented in Section VI.

II. INCORPORATING TUBE CLEARANCE

This section derives a kinematic model for concentric tube robots that incorporates the tube-to-tube clearance. The standard zero-clearance model is first reviewed in which all the tubes conform to a single centerline curve. Then the kinematics in the presence of clearance are formulated as an energy minimization by relaxing the single centerline assumption. An energy minimization is solved through a vector space optimization and its dual problem formulation. Finally the computational algorithms to solve the dual problem are presented. The variables used in the paper are enumerated in the Nomenclature. We remark that vectors are expressed with bold lower case letters, matrices are denoted by bold uppercase letters, and functions and scalar variables are denoted by either lower or uppercase nonbold italic letters.

A. Standard Zero-Clearance Kinematics

Consider a concentric tube robot with n tubes. The robot is parameterized with an arc-length parameter s along the length.

The tubes are numbered from the outermost one (tube 1) to the innermost one (tube n). Tube i has its own precurvature function $\hat{\mathbf{u}}_i(s) \in \mathbb{R}^{3 \times 1}$ and bending and torsional stiffness $k_{i,xy}, k_{i,z} \in \mathbb{R}$. The x - and y -components of $\hat{\mathbf{u}}_i(s)$ represent the bending curvature and the z -component represents the twist rate of the tube (e.g., rad/mm).

The existing mechanics-based kinematic model provides an elastic equilibrium of the tubes. The kinematics can be mathematically summarized as a map from base rotations and translations to the bending curvatures and torsional curvatures (twist rates) of the tubes [10], [11]:

1) input: (θ_b, \mathbf{l}_b)

2) output: $\mathbf{u}_i(s)$ for $s \in [l_{i,b}, l_{i,e}]$ and $i = 1, \dots, n$

where $\theta_b = [\theta_{1,b}, \theta_{2,b}, \dots]^T \in \mathbb{R}^n$ and $\mathbf{l}_b = [l_{1,b}, l_{2,b}, \dots]^T \in \mathbb{R}^n$ are the base rotations and translations of the tubes, respectively, and $\mathbf{u}_i(s) \in \mathbb{R}^3$ is the 3-D curvature function of tube i at the elastic equilibrium whose x - and y -components are the bending curvature, z -component is the torsional curvature, and $s = l_{i,e}$ is the distal end of tube i . The body frames and the centerline curves of the tubes $\mathbf{R}_i(s)$ and $\mathbf{p}_i(s)$ are then computed from $\mathbf{u}_i(s)$ by

$$\begin{aligned}\dot{\mathbf{R}}_i(s) &= \mathbf{R}_i(s)\langle \mathbf{u}_i(s) \rangle \\ \dot{\mathbf{p}}_i(s) &= \mathbf{R}_i(s)\hat{\mathbf{e}}_z\end{aligned}\quad (2)$$

with the boundary conditions

$$\begin{aligned}\mathbf{R}_i(l_{i,b}) &= \mathbf{R}_z(\theta_{i,b}) \\ \mathbf{p}_i(l_{i,b}) &= [0 \ 0 \ l_{i,b}]^T\end{aligned}\quad (3)$$

where $\hat{\mathbf{e}}_z = [0 \ 0 \ 1]^T$ and the upper dot represents the derivative with respect to s . Note that $\langle \cdot \rangle$ is the 3×3 skew symmetric matrix representation of 3-D vector and $\mathbf{R}_z(\theta) \in \mathbb{R}^{3 \times 3}$ is the rotation matrix of the frame rotated by θ about z -axis from $I_{3 \times 3}$. The solution of the kinematics satisfies $\mathbf{p}_i(s) = \mathbf{p}_j(s)$ for any tube i and tube j since this is one of the simplifying assumptions used in [10]–[13]. The computation of $\mathbf{u}_i(s)$ involves solving a set of differential equations, the details of which can be found in [10] and [11].

B. Kinematics in the Presence of Clearance

When there are clearances between tubes, the centerlines of the tubes can vary up to the limits prescribed by the clearances. Employing a potential energy formulation as in [12] and [13] and relaxing the assumption of a shared centerline, the mechanics of the tubes with nonzero clearances can be expressed as an infinite-dimensional optimization as follows:

$$\min_{\{\mathbf{u}_i(s)\}_{i=1,\dots,n}} \sum_{i=1}^n \int_{l_{i,b}}^{l_{i,e}} g_i(s) ds \quad (4)$$

where

$$g_i(s) = \frac{1}{2}(\mathbf{u}_i(s) - \hat{\mathbf{u}}_i(s))^T \mathbf{K}_i (\mathbf{u}_i(s) - \hat{\mathbf{u}}_i(s)) \quad (5)$$

subject to the contact constraints, i.e., each tube must remain inside its outer neighbor. Here, \mathbf{K}_i is a 3×3 diagonal matrix with $k_{i,xy}, k_{i,xy}$, and $k_{i,z}$ in the diagonal components.

C. Formulation as Vector Space Optimization

The optimization in the previous section can be converted to a vector space optimization by discretizing the arc length s and all functions of s . First, let vector $\vec{\mathbf{u}}_i$ and vector $\vec{\mathbf{p}}_i$ denote the collection of discretized $\mathbf{u}_i(s)$ and $\mathbf{p}_i(s)$, i.e.,

$$\begin{aligned}\vec{\mathbf{u}}_i &= [\mathbf{u}_i(s_{i1})^T \ \mathbf{u}_i(s_{i2})^T \ \dots]^T \in \mathbb{R}^{3N_i} \\ \vec{\mathbf{p}}_i &= [\mathbf{p}_i(s_{i1})^T \ \mathbf{p}_i(s_{i2})^T \ \dots]^T \in \mathbb{R}^{3N_i}\end{aligned}\quad (6)$$

and define vectors $\vec{\mathbf{u}}$ and $\vec{\mathbf{p}}$, the collections of $\vec{\mathbf{u}}_i$ and vector $\vec{\mathbf{p}}_i$ for all the tubes, as

$$\begin{aligned}\vec{\mathbf{u}} &= [\vec{\mathbf{u}}_1^T \ \vec{\mathbf{u}}_2^T \ \dots]^T \in \mathbb{R}^{3N} \\ \vec{\mathbf{p}} &= [\vec{\mathbf{p}}_1^T \ \vec{\mathbf{p}}_2^T \ \dots]^T \in \mathbb{R}^{3N}\end{aligned}\quad (7)$$

Here, $\{s_{ij}\}_{j=1,\dots,N_i}$ is the set of all the discretized points on tube i and N_i is the number of the points. To define them, the entire robot length is discretized first and then $\{s_{ij}\}_{j=1,\dots,N_i}$ is formed as the collection of all discretized points where tube i exists. Defining $\mathcal{S}_i = \{s_{ij}\}_{j=1,\dots,N_i}$ as the set of points for tube i , we note that $\mathcal{S}_1 \subset \mathcal{S}_2 \subset \dots \subset \mathcal{S}_n$ since inner tubes are longer and so are defined over a larger range of arc length than outer tubes. N is defined as the sum of N_i over all tubes, i.e., $N = \sum_{i=1}^n N_i$. Then, by (2) and (3), $\vec{\mathbf{p}}$ is a function of $\vec{\mathbf{u}}$, i.e.,

$$\vec{\mathbf{p}} = F(\vec{\mathbf{u}}). \quad (8)$$

The contact constraint can also be expressed as a set of inequalities imposed on a function of the vector $\vec{\mathbf{p}}$. For now, let us just write it by

$$G(\vec{\mathbf{p}}) \leq \mathbf{0}. \quad (9)$$

The numerical integration of the objective in (4) is also rewritten with the vector $\vec{\mathbf{u}}$ of the form

$$E = \frac{1}{2}(\vec{\mathbf{u}} - \vec{\mathbf{u}})^T \mathbf{K}(\vec{\mathbf{u}} - \vec{\mathbf{u}}) \quad (10)$$

where $\vec{\mathbf{u}} \in \mathbb{R}^{3N}$ is the discretized precurvature vectorized from $\{\hat{\mathbf{u}}_i(s)\}_{i=1,\dots,n}$ in the same way as $\vec{\mathbf{u}}$, and $\mathbf{K} \in \mathbb{R}^{3N \times 3N}$ is a diagonal matrix whose i th diagonal component is the bending or torsional stiffness (\times arc length step) associated with the i th component of the curvature vector u . For example, the first and the second diagonal components of K are $k_{1,xy} \Delta s$ and the third component is $k_{1,z} \Delta s$, where Δs is the step size in the arc-length discretization. Note that the torsional stiffness of tube i , $k_{i,z}$, is computed by $k_{i,z} = k_{i,xy}/(1 + \nu)$, where $k_{i,xy}$ and ν are the bending stiffness and the Poisson's ratio, respectively. The energy function (10) thus is the potential energy of all the tubes induced by both bending and twist.

Despite the convex objective function, this problem is not convex because the contact constraint is nonconvex. By assuming small clearances and, accordingly, small differences in the tube curvatures from the solution of the zero-clearance model introduced at the beginning of Section II, the optimization reduces to a convex problem by linearizing (8).

Let $\{\mathbf{u}_i^*(s), \mathbf{R}_i^*(s), \mathbf{p}_i^*(s)\}_{i=1,\dots,n}$ denote an initial guess of the solution about which the system will be linearized. The solution of the zero-clearance model, for example, can

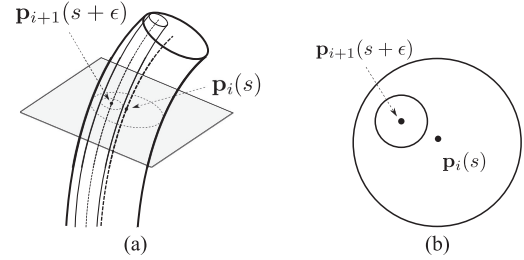


Fig. 2. Intersection of inner tube with cross section of outer tube. (a) Centerlines. (b) Plane of cross section.

be considered as the initial guess. Let $\vec{\mathbf{u}}_i^*, \vec{\mathbf{p}}_i^* \in \mathbb{R}^{3N_i}$, and $\vec{\mathbf{u}}^*, \vec{\mathbf{p}}^* \in \mathbb{R}^{3N}$ denote the discretized version of this solution following the notation of (6) and (7). Define $\Delta\vec{\mathbf{u}}_i, \Delta\vec{\mathbf{p}}_i \in \mathbb{R}^{3N_i}$ and $\Delta\vec{\mathbf{u}}, \Delta\vec{\mathbf{p}} \in \mathbb{R}^{3N}$ as the small changes in the curvatures and the centerlines from the initial guess as follows:

$$\begin{aligned}\vec{\mathbf{u}} &= \vec{\mathbf{u}}^* + \Delta\vec{\mathbf{u}} \quad \vec{\mathbf{p}} = \vec{\mathbf{p}}^* + \Delta\vec{\mathbf{p}} \\ \vec{\mathbf{u}}_i &= \vec{\mathbf{u}}_i^* + \Delta\vec{\mathbf{u}}_i \quad \vec{\mathbf{p}}_i = \vec{\mathbf{p}}_i^* + \Delta\vec{\mathbf{p}}_i.\end{aligned}\quad (11)$$

Substituting (11) in the objective (10) and omitting the constant term yields

$$\min_{\Delta\vec{\mathbf{u}}} \left(\frac{1}{2} \Delta\vec{\mathbf{u}}^T \mathbf{K} \Delta\vec{\mathbf{u}} + \mathbf{g}^T \Delta\vec{\mathbf{u}} \right) \quad (12)$$

where \mathbf{g} is defined by

$$\mathbf{g} = \mathbf{K}(\vec{\mathbf{u}}^* - \vec{\mathbf{u}}^*). \quad (13)$$

Now let us focus on the contact constraint. Consider the cross section of the robot at $\mathbf{p}_i(s)$ as shown in Fig. 2. The cross section intersects with $\mathbf{p}_{i+1}(s + \epsilon)$, not $\mathbf{p}_{i+1}(s)$, since integrating along the different centerlines results in different arc lengths on the cross section. The quantity ϵ is this arc-length difference. While we assume the tubes have circular cross sections, the intersection of the inner tube with the cross-sectional plane of the outer tube in Fig. 2(b) would not be a circle since the tubes are angled from each other. However, it is still possible to approximate it as a circle based on the small clearance assumption. The constraint can then be written as

$$\|\mathbf{p}_i(s) - \mathbf{p}_{i+1}(s + \epsilon)\| \leq c_i \quad (14)$$

where the clearance $c_i (i = 1, \dots, n)$ is given by

$$c_i = r_{i,\text{in}} - r_{i+1,\text{out}} \quad (15)$$

where $r_{i,\text{in}}$ and $r_{i,\text{out}}$ are the inner and outer radii of tube i , respectively.

Assuming small ϵ , the first-order approximation of $\mathbf{p}_i(s) - \mathbf{p}_{i+1}(s + \epsilon)$ is given by

$$\mathbf{p}_i(s) - \mathbf{p}_{i+1}(s + \epsilon) \approx \mathbf{p}_i(s) - \mathbf{p}_{i+1}(s) - \epsilon \dot{\mathbf{p}}_{i+1}^*(s). \quad (16)$$

Since (16) is a vector on the cross-sectional plane, the projection of this vector onto the plane is the vector itself, shown as follows:

$$\begin{aligned}\mathbf{p}_i(s) - \mathbf{p}_{i+1}(s) - \epsilon \dot{\mathbf{p}}_{i+1}^*(s) &= \mathbf{P}_i(s)(\mathbf{p}_i(s) - \mathbf{p}_{i+1}(s) \\ &\quad - \epsilon \dot{\mathbf{p}}_{i+1}^*(s))\end{aligned}\quad (17)$$

where the projection matrix is approximated with $\dot{\mathbf{p}}^*(s)$, i.e.,

$$\mathbf{P}_i(s) \approx \mathbf{I}_{3 \times 3} - \dot{\mathbf{p}}_i^*(s)\dot{\mathbf{p}}_i^*(s)^T. \quad (18)$$

Noting that $\mathbf{P}_i(s)\dot{\mathbf{p}}_{i+1}^*(s)$ is a small vector since $\dot{\mathbf{p}}_{i+1}^*(s) \approx \dot{\mathbf{p}}_i^*(s)$ for small clearances and $\dot{\mathbf{p}}_i^*(s)$ is a null vector of $\mathbf{P}_i(s)$, the last term on the right side of (17) $\epsilon \mathbf{P}_i(s)\dot{\mathbf{p}}_{i+1}^*(s)$ is a second-order term. Neglecting this term, the contact constraint (14) reduces to

$$(\mathbf{p}_i(s) - \mathbf{p}_{i+1}(s))^T \mathbf{P}_i(s)(\mathbf{p}_i(s) - \mathbf{p}_{i+1}(s)) \leq c_i^2. \quad (19)$$

This inequality needs to be evaluated on the discretized points where both tube i and tube $i + 1$ exist. This can be done by substituting $s = s_{ij}$ into (19) and the resulting inequality can be now expressed with the vector $\vec{\mathbf{p}}$ of the form

$$\vec{\mathbf{p}}^T \mathbf{S}_{ij}^T \mathbf{P}_{ij} \mathbf{S}_{ij} \vec{\mathbf{p}} \leq c_i^2 \quad (20)$$

for all $i = 1, \dots, n - 1$, $j = 1, \dots, N_i$ where $\mathbf{S}_{ij} \in \mathbb{R}^{3 \times 3N}$ is a selection matrix to pick $\mathbf{p}_i(s_{ij})$ and $-\mathbf{p}_{i+1}(s_{ij})$ from $\vec{\mathbf{p}}$ such that

$$\mathbf{S}_{ij} \vec{\mathbf{p}} = \mathbf{p}_i(s_{ij}) - \mathbf{p}_{i+1}(s_{ij}) \quad (21)$$

and $P_{ij} \in \mathbb{R}^{3 \times 3}$ is a projection matrix given by

$$\mathbf{P}_{ij} = \mathbf{I}_{3 \times 3} - \dot{\mathbf{p}}_i^*(s_{ij})\dot{\mathbf{p}}_i^*(s_{ij})^T. \quad (22)$$

Linearizing (8) in terms of $\Delta\vec{\mathbf{p}}$ and $\Delta\vec{\mathbf{u}}$,

$$\Delta\vec{\mathbf{p}} = \mathbf{J}_p \Delta\vec{\mathbf{u}} \quad (23)$$

where $\mathbf{J}_p = \partial F / \partial \vec{\mathbf{u}} \in \mathbb{R}^{3N \times 3N}$. The matrix \mathbf{J}_p maps small changes in tube curvatures to the corresponding changes in the tube centerlines. The analytic form of \mathbf{J}_p is presented in Appendix B. Finally, the constraint (20) can be expressed as a convex constraint with respect to $\Delta\vec{\mathbf{u}}$ by combining (20) with $\vec{\mathbf{p}}$ and $\Delta\vec{\mathbf{p}}$ from (11) and (23), as follows:

$$G_{ij}(\Delta\vec{\mathbf{u}}) := \frac{1}{2} \Delta\vec{\mathbf{u}}^T \mathbf{X}_{ij}^T \mathbf{X}_{ij} \Delta\vec{\mathbf{u}} + \mathbf{x}_{ij}^T \mathbf{X}_{ij} \Delta\vec{\mathbf{u}} + q_{ij} \leq 0 \quad (24)$$

where X_{ij} , \mathbf{x}_{ij} , and q_{ij} are given by

$$\begin{aligned} \mathbf{X}_{ij} &= \mathbf{P}_{ij} \mathbf{S}_{ij} \mathbf{J}_p \in \mathbb{R}^{3 \times 3N} \\ \mathbf{x}_{ij} &= \mathbf{P}_{ij} \mathbf{S}_{ij} \vec{\mathbf{p}}^* \in \mathbb{R}^{3 \times 1} \\ q_{ij} &= 1/2 (\mathbf{x}_{ij}^T \mathbf{x}_{ij} - c_i^2) \in \mathbb{R}. \end{aligned} \quad (25)$$

Now the problem consists of a convex objective function and a set of convex constraints. This is, however, computationally difficult to solve using a standard iterative optimization involving gradient descent and projection onto the constraint manifold owing to the high dimensionality of $\Delta\vec{\mathbf{u}}$ and the large number of nonlinear constraints. For this reason, we recast the problem as its dual [23] to reduce its dimensionality and produce linear constraints.

D. Dual Problem Formulation

The dual problem involves optimizing over Lagrange multipliers associated with the constraints of the original problem. The dimensionality of the dual problem is thus equal to the number of constraints in the original problem. The dual problem is

a maximization and its objective function is always concave while the constraints are linear since the multipliers are nonnegative. For example, the three-tube robot design appearing later in the paper is of dimension 630 and involves 133 nonlinear constraints when the innermost tube is fully extended. In its dual formulation, the dimensionality is reduced to 133 with 133 linear constraints. Furthermore, it has been shown that the dual problem attains the global solution of the original problem if the original problem was convex [23].

Following [23], the dual problem is given as the following maximization:

$$\max_{\lambda} \left\{ E_{\lambda} = \frac{1}{2} \mathbf{h}(\lambda)^T \mathbf{Q}(\lambda)^{-1} \mathbf{h}(\lambda) - \mathbf{q}^T \lambda \right\} \quad (26)$$

subject to

$$\lambda_k \geq 0 \text{ for } k = 1, \dots, M \quad (27)$$

where $\lambda = [\lambda_1 \ \lambda_2 \ \dots]^T$ is an M -dimensional vector and M is the number of constraints, i.e., $M = \sum_{i=1}^{n-1} N_i$. $\mathbf{Q}(\lambda)$ and $\mathbf{h}(\lambda)$ are defined as

$$\mathbf{Q}(\lambda) = \mathbf{K} + \sum_{k=1}^M \lambda_k \mathbf{X}_k^T \mathbf{X}_k \quad (28)$$

$$\mathbf{h}(\lambda) = \mathbf{g} + \sum_{k=1}^M \lambda_k \mathbf{X}_k^T \mathbf{x}_k \quad (29)$$

where \mathbf{X}_k and \mathbf{x}_k are renumbered with the index k from \mathbf{X}_{ij} and \mathbf{x}_{ij} , respectively. The gradient of E_{λ} is then analytically given by

$$\frac{\partial E_{\lambda}}{\partial \lambda_k} = G_k(\Delta\vec{\mathbf{u}}) \quad (30)$$

where G_k is renumbered from G_{ij} in (24) and $\Delta\vec{\mathbf{u}}$ is given by

$$\Delta\vec{\mathbf{u}} = \mathbf{Q}(\lambda)^{-1} \mathbf{h}(\lambda). \quad (31)$$

This can be computed by solving the linear equation

$$\mathbf{Q}(\lambda) \Delta\vec{\mathbf{u}} = \mathbf{h}(\lambda) \quad (32)$$

for a given \mathbf{Q} and \mathbf{h} . An efficient way of solving this equation using the matrix inversion lemma is given in Appendix A.

Gradient ascent with constraint projection works nicely with this problem thanks to the linear constraints (27). The projection of λ onto the violated constraints can be done simply by setting all $\lambda_k < 0$ to be $\lambda_k = 0$.

Physically, these multipliers are proportional to the contact forces concentrated at the corresponding points. The force $f_k \in \mathbb{R}$ can be derived as

$$f_k = c_i \lambda_k \text{ for } k = 1, \dots, M \quad (33)$$

based on a virtual displacement and energy analysis. Here, c_i is the clearance of the tube pair associated with the k th contact constraint. Note that, since we have discretized the arc length, distributed contact forces are computed as sets of neighboring concentrated forces.

E. Computation of Clearance Model

The algorithm to solve the dual problem optimization is as follows. Given an initial guess $\{(\mathbf{u}_i^*(s), R_i^*(s), \mathbf{p}_i^*(s))\}_{i=1,\dots,n}$, the initialization steps include:

- 1) constructing matrix K based on the stiffnesses of the tubes,
- 2) computing \mathbf{g} from (13),
- 3) computing \mathbf{J}_p as given in Appendix B,
- 4) computing $q_k (= q_{ij})$, $\mathbf{X}_k^T \mathbf{X}_k (= \mathbf{X}_{ij}^T \mathbf{X}_{ij})$ and $\mathbf{X}_k^T \mathbf{x}_k (= \mathbf{X}_{ij}^T \mathbf{x}_{ij})$ from (25),
- 5) initializing λ .

The optimization loop is as follows:

- 1) Compute \mathbf{Q} and \mathbf{h} from (28) and (29) using the current values of λ
- 2) Solve $\mathbf{Q}\Delta\vec{\mathbf{u}} = \mathbf{h}$ for $\Delta\vec{\mathbf{u}}$.
- 3) Compute $\mathbf{d} = \frac{\partial E_\lambda}{\partial \lambda}^T$ in (30) using $\Delta\vec{\mathbf{u}}$ computed in 2).
- 4) Update λ by $\lambda \leftarrow \lambda + \delta \mathbf{d}$ with a small positive scalar δ .
- 5) For all k , set $\lambda_k = 0$ if $\lambda_k < 0$.
- 6) Check convergence and terminate the loop if converged.
- 7) Otherwise, go back to 1).

The convergence can be checked based on the change in λ_k between two consecutive iterations. Once converged, the latest $\Delta\vec{\mathbf{u}}$ can be added to $\vec{\mathbf{u}}^*$ to compute the new tube curvatures. A good initial guess $\{(\mathbf{u}_i^*(s), R_i^*(s), \mathbf{p}_i^*(s))\}_{i=1,\dots,n}$ can be given from the standard zero-clearance model. Recalling that the tube centerline change $\Delta\vec{\mathbf{p}}$ is assumed linear to $\Delta\vec{\mathbf{u}}$ by (23), the solution obtained through this optimization is an approximation. The solution can then be refined by substituting itself as a new initial guess and running the optimization loop again. This can be implemented as an outer loop that encloses the optimization loop as an inner loop. The computational steps of the outer loop are given below:

- 1) Set $\{(\mathbf{u}_i^*(s), R_i^*(s), \mathbf{p}_i^*(s))\}_{i=1,\dots,n}$ as the solution of the standard zero-clearance model.
- 2) Compute $\Delta\vec{\mathbf{u}}$ through the above optimization for given $\{(\mathbf{u}_i^*(s), R_i^*(s), \mathbf{p}_i^*(s))\}_{i=1,\dots,n}$.
- 3) Terminate the loop if $\|\Delta\vec{\mathbf{u}}\|$ is small, i.e., $\|\Delta\vec{\mathbf{u}}\| < \gamma$ for a small positive γ .
- 4) Update $\vec{\mathbf{u}}^*$ by $\vec{\mathbf{u}}^* \leftarrow \vec{\mathbf{u}}^* + \alpha \Delta\vec{\mathbf{u}}$ for a positive real α .
- 5) Update $\{(\mathbf{u}_i^*(s), R_i^*(s), \mathbf{p}_i^*(s))\}_{i=1,\dots,n}$ by (2) and (3) using $\vec{\mathbf{u}}^*$ and go back to 2).

For the three-tube robot design used in the simulations and experiments, the values of δ , α , and γ are chosen to be $\delta = 10^{-3}$, $\alpha = 1.0$, and $\gamma = 10^{-6}$ for stable convergence. The inner loop usually runs for hundreds to thousands of iterations and the outer loop runs for tens of iterations. The initial λ_k was chosen as a positive constant, such as $\lambda = [1, 1, 1, \dots]^T$, and then the final λ in the previous optimization loop is used as the initial λ in the following loop.

III. MODELING MAXIMUM TORSIONAL FRICTION

We now seek to model the configurations in which intertube friction either maximizes or minimizes the relative angular twist between tube pairs. To do so, we assume that the path history is such that Coulomb friction is producing its maximum force

at each point of contact along the length of the tube pairs (i.e., the friction coefficient multiplied by the local normal force) and that this force is entirely directed so as to oppose tube twisting (i.e., there is no component in the direction of translation).

With friction, the system is no longer conservative and so its model cannot be formulated directly by energy minimization. We can, however, introduce friction into the model derived above. Consider that the dual problem in Section II-D can be interpreted as solving for equilibrium of a mechanical system of elastic rods under interaction forces between tubes. To see this, substitute (11), (13), (25), (28), and (29) into (32), which yields

$$\mathbf{K}(\vec{\mathbf{u}} - \vec{\mathbf{u}}^*) = \mathbf{J}_p^T \mathbf{f}_{\text{normal}} \quad (34)$$

where

$$\mathbf{f}_{\text{normal}} = \sum_{k=1}^M \mathbf{S}_k^T \mathbf{f}_{\text{normal},k} \in \mathbb{R}^{3N \times 1} \quad (35)$$

$$\mathbf{f}_{\text{normal},k} = -\lambda_k \mathbf{P}_k \mathbf{S}_k \vec{\mathbf{p}} \in \mathbb{R}^{3 \times 1}. \quad (36)$$

Here $\mathbf{f}_{\text{normal},k}$ is the normal force applied on the outer tube associated with the k th contact constraint, whose magnitude becomes f_k in (33) once λ converges. Then \mathbf{S}_k^T in (35) applies this force on both the inner and outer tubes with the opposing directions. Note that $\mathbf{f}_{\text{normal}}$ is a vector comprised of the forces applied on all the discretized points of the tubes and the left side of (34) is a vector comprised of all the elastic moments on the same set of points. In a robotics context, (34) is an equation of static equilibrium between the elastic moments of the tubes and the normal forces on the tubes [24].

Our goal in this section is to reformulate the equilibrium (34) to include the tube-to-tube friction forces and torques in the form

$$K(\vec{\mathbf{u}} - \vec{\mathbf{u}}^*) = \mathbf{J}_p^T \mathbf{f} + \mathbf{J}_\omega^T \boldsymbol{\tau} \quad (37)$$

so as to solve for the equilibrium in the presence of the friction. Here \mathbf{f} is a vector comprised of forces that include both the normal contact forces and the friction forces, $\boldsymbol{\tau}$ is a vector of the friction torques and \mathbf{J}_ω is a Jacobian matrix of $\mathbf{R}_i(s)$ with respect to $\vec{\mathbf{u}}$ derived in Appendix B. Physically the Jacobian matrix \mathbf{J}_ω is the linear map from small changes in tube curvatures to the corresponding angular displacements in the tube body frames. This formulation leads to new forms of $\mathbf{Q}(\lambda)$ and $\mathbf{h}(\lambda)$ different from (28) and (29).

Noting that \mathbf{J}_p is the differentiation of F in (8), \mathbf{J}_p transforms body-frame curvature changes to world-frame centerline changes. Thus, the force vector \mathbf{f} is to be expressed in the world frame. The Jacobian matrix \mathbf{J}_ω is derived in Appendix B to convert body-frame curvature changes to body-frame rotations of the frames $\mathbf{R}_i(s)$. Consequently, the torque vector $\boldsymbol{\tau}$ is to be expressed in the body frame.

Now, the force \mathbf{f} and the torque $\boldsymbol{\tau}$ will be derived accordingly. Focusing on the k th contact constraint, the friction force lies on the plane perpendicular to the normal force $\mathbf{f}_{\text{normal},k}$. Assuming that the entirety of the friction force is directed toward tube twisting, the friction force can be computed by the cross product of the tangent vector of the tube centerline and the normal force $\mathbf{f}_{\text{normal},k}$. Assuming that the path history is such that the

maximum friction force magnitude is being applied at each point of contact, its magnitude is proportional to $\mathbf{f}_{\text{normal},k}$ with the friction coefficient μ_k . Finally, the friction force is expressed as

$$\mathbf{f}_{\text{friction},k} = \eta_k \mu_k \langle \dot{\mathbf{p}}_i^*(s_k) \rangle \mathbf{f}_{\text{normal},k} \quad (38)$$

where $\dot{\mathbf{p}}_i^*(s_k)$ is an approximation of the tangent vector of the outer tube (tube i) given by the initial solution, $s_k (= s_{ij})$ is where the k th contact constraint is defined, and η_k decides the direction of the friction force depending on the prior relative base rotation between the tubes associated with the k th contact constraint. Here, η_k is defined as

$$\eta_k = \begin{cases} +1 & \text{for CCW prior rotation} \\ -1 & \text{for CW prior rotation} \end{cases} \quad (39)$$

where counterclockwise (CCW) and clockwise (CW) rotations are defined by the inner tube rotation relative to the outer tube. Again, the bracket $\langle \cdot \rangle$ in (38) indicates the 3×3 skew symmetric matrix.

Adding this friction force to (35) yields

$$\mathbf{f} = \sum_{k=1}^M \mathbf{S}_k^T (\mathbf{I}_{3 \times 3} + \eta_k \mu_k \langle \dot{\mathbf{p}}_i^*(s_k) \rangle) \mathbf{f}_{\text{normal},k}. \quad (40)$$

Now the body-frame expression of the friction torques will be given. Since the friction torques are applied about the tube's central axis, i.e., the z -axis of $\mathbf{R}_i(s)$, the body-frame expression of the torque is simply the z -vector $\hat{\mathbf{e}}_z = [0 \ 0 \ 1]^T$ multiplied with a scalar that represents the magnitude of the torque. The torque magnitude is computed as a multiplication of the contact force magnitude, the friction coefficient, and the tube radius. Using the scalar representation of the contact force in (33), the friction torques on the outer and inner tubes are given respectively by

$$\begin{aligned} \boldsymbol{\tau}_{i,k} &= \eta_k r_{i,\text{in}} \mu_k f_k \hat{\mathbf{e}}_z \in \mathbb{R}^{3 \times 1} \\ \boldsymbol{\tau}_{i+1,k} &= -\eta_k r_{i+1,\text{out}} \mu_k f_k \hat{\mathbf{e}}_z \in \mathbb{R}^{3 \times 1} \end{aligned} \quad (41)$$

where f_k is defined in (33) and η_k decides the direction again based on the relative tube rotation. The collection of $\boldsymbol{\tau}_{k,\text{in}}$ and $\boldsymbol{\tau}_{k,\text{out}}$ over all $k = 1, \dots, M$ is given by

$$\boldsymbol{\tau} = \sum_{k=1}^M c_i \lambda_k \mathbf{W}_k \mathbf{S}_k^T \hat{\mathbf{e}}_z \in \mathbb{R}^{3N \times 1} \quad (42)$$

where \mathbf{W}_k is given by

$$\mathbf{W}_k = \begin{bmatrix} \mathbf{W}_{1,k} & & 0 \\ & \ddots & \\ 0 & & \mathbf{W}_{n,k} \end{bmatrix} \in \mathbb{R}^{3N \times 3N} \quad (43)$$

where the i th and $i + 1$ st diagonal blocks are nonzero matrices, $\mathbf{W}_{i,k} = \eta_k r_{i,\text{in}} \mu_k \mathbf{I}_{3N_i \times 3N_i}$ and $\mathbf{W}_{i+1,k} = \eta_k r_{i+1,\text{out}} \mu_k \mathbf{I}_{3N_{i+1} \times 3N_{i+1}}$ and all the others are zero matrices, i.e., $\mathbf{W}_{j,k} = \mathbf{0}_{3N_j \times 3N_j}$ for $j \neq i, i + 1$. Here, i and $i + 1$ are the indices of the tubes involved in the k th contact constraint.

By substituting (40) and (42) into (37) and after an algebraic manipulation, the moment equilibrium (37) reduces again to

$$\mathbf{Q}(\lambda) \Delta \vec{\mathbf{u}} = \mathbf{h}(\lambda) \quad (44)$$

TABLE I
PARAMETERS OF TUBE PAIR

	Tube 1		Tube 2	
	Section 1	Section 2	Section 1	Section 2
Length (mm)	150	17	150	150
Curvature (mm^{-1})	1/150	0.0	1/150	1/150
Bending Stiffness (Nm^2)	5.07×10^{-2}	5.07×10^{-2}	5.07×10^{-2}	5.07×10^{-2}
Poisson's ratio	0.3	0.3	0.3	0.3
OD \ ID (mm)	$-\sqrt{1.02} - 7.0$	$1.0\sqrt{-}$	$-\sqrt{1.02} - 7.0$	$1.0\sqrt{-}$
Clearance (mm)	0.01 - 3.0		0.01 - 3.0	
Friction coefficient	0.0 - 0.5		0.0 - 0.5	

TABLE II
PARAMETERS OF THREE-TUBE ROBOT

	Tube 1		Tube 2		Tube 3	
	Section 1	Section 2	Section 1	Section 2	Section 1	Section 2
Length (mm)	150	17	150	184	86.4	86.4
Curvature (mm^{-1})	1/265	0.0	1/265	0.0	1/55	1/55
Bending Stiffness (Nm^2)	5.07×10^{-2}	5.07×10^{-2}	5.07×10^{-2}	1.45×10^{-2}	1.45×10^{-2}	1.45×10^{-2}
Poisson's ratio	0.3	0.3	0.3	0.3	0.3	0.3
OD \ ID (mm)	$-\sqrt{2.39}$	$2.305\sqrt{1.95}$	1.95	1.95	$1.825\sqrt{-}$	$1.825\sqrt{-}$
Clearance (mm)	0.0425		0.0625		0.0625	
Friction Coefficient	0.2		0.2		0.2	

for new $\mathbf{Q}(\lambda)$ and $\mathbf{h}(\lambda)$ given by

$$\mathbf{Q}(\lambda) = \mathbf{K} + \sum_{k=1}^M \lambda_k \mathbf{Y}_k^T \mathbf{X}_k \quad (45)$$

$$\mathbf{h}(\lambda) = \mathbf{g} + \mathbf{J}_\omega^T \boldsymbol{\tau} + \sum_{k=1}^M \lambda_k \mathbf{Y}_k^T \mathbf{x}_k \quad (46)$$

where

$$\mathbf{Y}_k = \mathbf{P}_k (\mathbf{I}_{3 \times 3} - \mu_k \langle \dot{\mathbf{p}}_i(s_k) \rangle) \mathbf{S}_k \mathbf{J}_p. \quad (47)$$

Equation (44) is the same form with (34) but $Q(\lambda)$ and $\mathbf{h}(\lambda)$ are now in different forms. Replacing (28) and (29) with (45) and (46) in the algorithm of Section II-E results in the solution that incorporates friction. In the inner loop initialization, as a result, \mathbf{J}_ω as well as \mathbf{J}_p needs to be computed and $\mathbf{X}_k^T \mathbf{X}_k$ and $\mathbf{X}_k^T \mathbf{x}_k$ are replaced with $\mathbf{Y}_k^T \mathbf{X}_k$ and $\mathbf{Y}_k^T \mathbf{x}_k$, respectively.

IV. NUMERICAL EXPERIMENTS

To understand how clearance and friction influence robot kinematics and contact force distribution, two designs of concentric tube robots were investigated in a series of numerical experiments: 1) a balanced tube pair and 2) a three-tube robot. Tube parameters are given in Tables I and II.

Note that the analysis is independent of the outer diameter (OD) of the outermost tube (tube 1) and the inner diameter (ID) of the innermost tube (tube n). These parameters are marked as “ $-$ ” in the tables.

The tubes for each design are shown in Fig. 3. The collars shown at the proximal ends of the tubes are required to mount the tubes in the drive system and have a length of 17 mm. The constraints introduced by the collars are included in the analysis. While any integration method can be used, the results presented here were computed using Euler integration, which implies that the discretized values are interpolated as constant between adjacent discretized points.

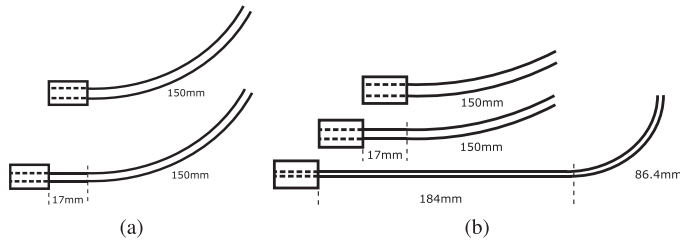


Fig. 3. Robot designs comprised of (a) a tube pair and (b) three tubes. The dashed lines indicate boundaries between straight and curved tube sections.

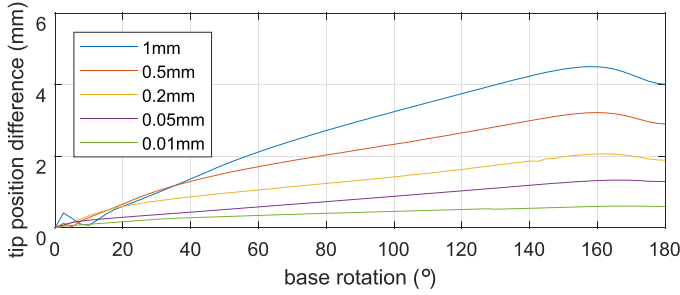


Fig. 4. Difference in tip position compared to zero-clearance model. The curves are plotted for 5° increments of the base rotation.

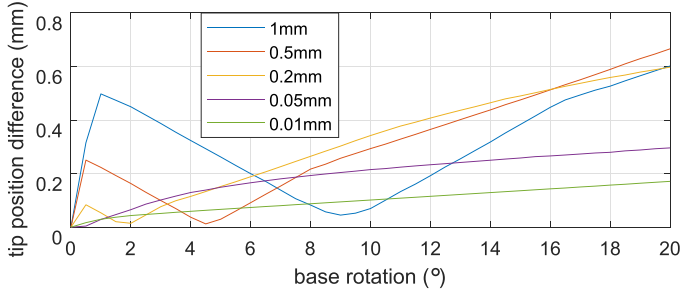


Fig. 5. Difference in tip position compared to zero-clearance model for small values of base rotation angle. The curves are plotted for 0.5° increments of the base rotation.

A. Effect of Clearance and Friction on Tip Position

Using the tube pair, we first investigated the effect of clearance alone on robot tip position, where tip position is measured for the inner robot tube. Fig. 4 compares the tip position computed for five values of clearance with the position predicted by the standard zero-clearance model. The difference in tip position is plotted as a function of base rotation angle. Tip position difference tends to increase with increasing clearance and base rotation, with the maximum differences occurring for values less than 180° . This is a more accurate result than was reported in [16], where the linearization (23) was performed only once.

We note that the nonsmooth portions of the curves at small base rotation angles, magnified in Fig. 5, are due to the mounting collars. This effect is explained below in Section IV-B.

While reducing clearance increases the accuracy of the zero-clearance model, it can be anticipated that the effect of friction between the tubes will be larger for smaller clearances. This

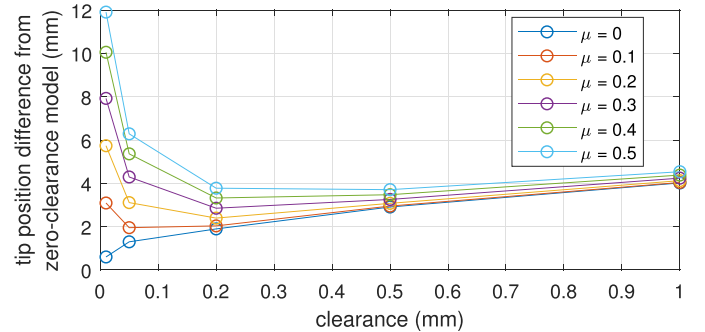


Fig. 6. Difference in tip position compared to zero-clearance model for a tube pair base angle of 180° as a function of clearance and friction coefficient.

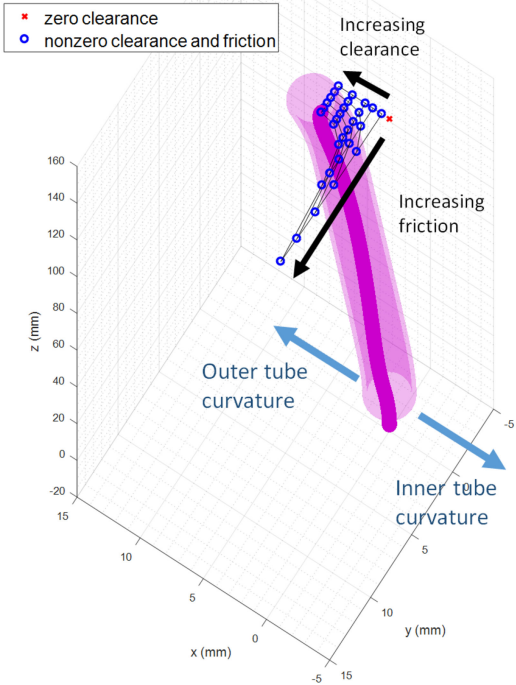


Fig. 7. Tip position of a tube pair as a function of clearance and friction coefficient. Base rotation angle is 180° . The illustrated tube shapes are for a clearance of 1.0 mm and a friction coefficient of 0.5.

is demonstrated in Fig. 6 which depicts tip position difference as a function of clearance for a tube pair base angle of 180° considering five values of friction coefficient.

Fig. 7 graphically illustrates how tip position varies with clearance and friction coefficient. In the depicted configuration, the zero-clearance frictionless model would predict the tubes to be straight along their entire length. With clearance, however, the tip moves in the direction of the outer tube curvature as the clearance increases. This is due to the mounting collars as explained in the following section. Friction produces tip displacements in the perpendicular direction. This is due to the fact that friction reduces rotation of the tubes along their length. As expected, the small clearance case is more influenced by the friction.

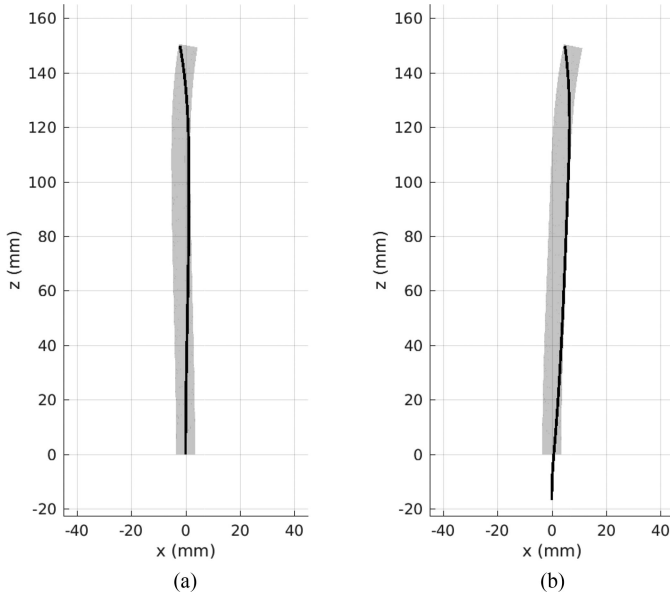


Fig. 8. Inner (black) and outer (gray) tubes in the presence of 3 mm clearance with (a) no straight transmission length and (b) a 17-mm straight transmission length of the inner tube. The tube centerlines in (b) are not symmetric due to the transmission length.

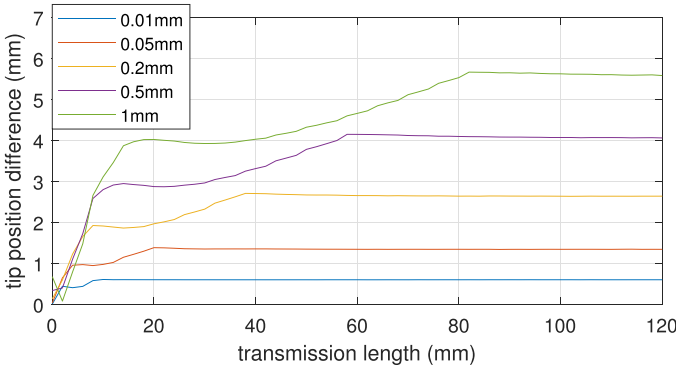


Fig. 9. Difference in tip position compared to zero-clearance model as a function of transmission length for five values of clearance.

B. Effect of Clearance in Modeling the Effect of Collars and Straight Transmission Lengths

Fig. 8 compares constant-curvature tube pairs for a base rotation angle of 180° with and without a straight transmission length on the inner tube to accommodate a collar for drive system mounting. The clearance in this figure is 3 mm, which is selected for ease of visualization. When there is no transmission length, the centerlines of the tubes are symmetric with respect to the z-axis as shown in Fig. 8(a). In contrast, when the inner tube has a transmission length, the inner tube comes into the outer tube with a nonzero angle causing the centerline of the inner tube to be shifted in the direction of the outer tube's pre-curvature as shown in Fig. 8(b). This results in the overall tube pair bending toward the positive x-direction.

To show how tip position varies with transmission length and clearance, tip position difference with respect to the zero clearance/zero transmission length model is plotted in Fig. 9 for varying transmission length and a discrete set of clearances. The

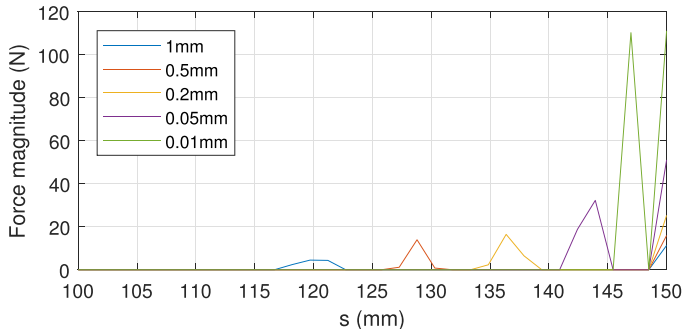


Fig. 10. Contact force magnitude versus arc length near tube tips for five values of clearance.

plotting range for transmission length in the figure is limited to elastically stable lengths based on [13] and [25].

In Fig. 5, it was observed that for small rotation angles, the tip position difference first increases, then decreases, and then increases again. This can be explained as follows. Initially, the tips of both tubes diverge from the tip position predicted by zero-clearance model and are relatively symmetric with respect to the tip position predicted by the zero-clearance model. When the interaction between the tubes becomes significant, the outer starts pulling the inner tube toward itself and the tip of inner tube passes by through tip position predicted by the zero-clearance model. Then, as the base rotation goes to 180° , the tip position differences of both tubes increase as the overall shapes approach to the shapes of Fig. 8(b).

C. Effect of Clearance and Friction on Contact Force Distribution

When the base of a tube pair is rotated away from 0° , the standard zero-clearance model predicts a concentrated moment applied between the tubes at their tips. With the inclusion of tube clearance, this concentrated moment is produced by a point force at the tip acting in combination with an oppositely directed force distribution located close to, but not at, the tip. To see the effect of clearance on the magnitudes and the distances between the two forces comprising this moment, the forces in the frictionless case are plotted as a function of arc length for $\theta_{2,b} = 180^\circ$ in Fig. 10. Note that, due to discretization, distributed forces are modeled as concentrated forces applied at the discretization points. As the clearance decreases, the forces increase in magnitude and approach each other so as to produce approximately the same net moment around 0.338 Nm. This is the moment required to straighten each of the tubes, which can be computed as bending stiffness \times curvature.

The distribution of the contact forces and their magnitudes vary with the base rotation. As base rotation angle increases from zero to 180° , the contact forces increase in magnitude and move toward the ends of the tubes. This is shown in Fig. 11, where the contact forces are depicted as green circles with diameters indicating magnitude of force. The green circle at the tip grows as the base rotates. These force magnitudes are plotted versus arc length in Fig. 12 for a superset of base rotation angles. Note

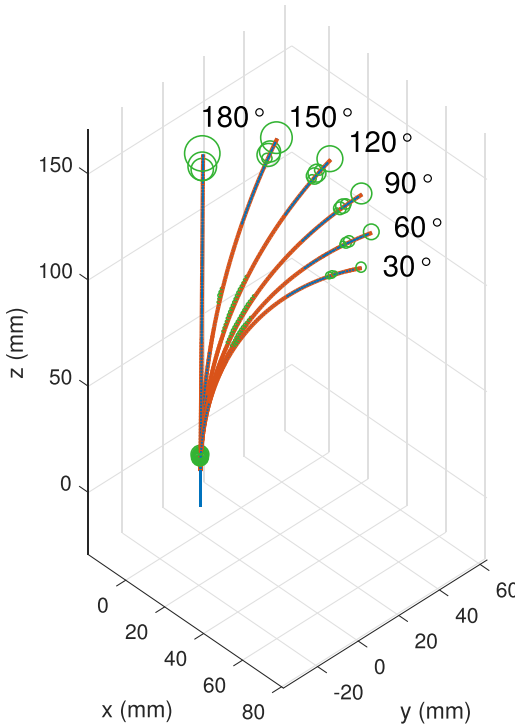


Fig. 11. Force distribution and magnitude as a function of base rotation angle for a clearance of 0.05 mm. Contact forces are visualized as green circles with diameters proportional to force magnitude.

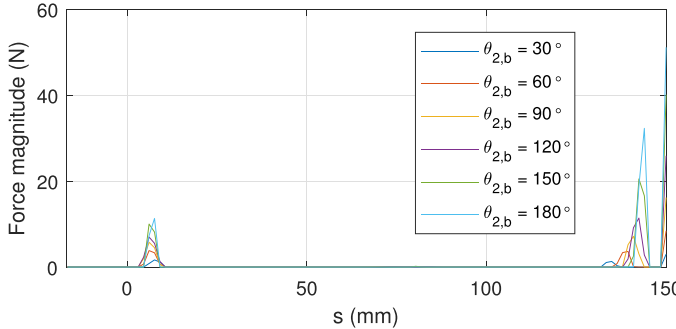


Fig. 12. Contact force magnitude as a function of arc length for six values of base rotation angle and a clearance of 0.05 mm.

that a third contact region near the base is also shown. The clearance is 0.05 mm in both figures.

The effect of friction on the contact force distributions is shown in Fig. 13 for a base rotation angle of 180°. Here, the contact forces magnitudes include both the normal and friction components. Even so, the force magnitudes are slightly reduced. This is due to the fact that friction reduces tube rotation leading to less tube straightening near the tips. Since the tip forces are required to straighten the tubes, they are also reduced.

D. Effect of Clearance and Friction on Tip Position of Three-Tube Robot

Consider the three-tube robot illustrated in Fig. 3(b) with parameters given in Table II. Assuming the base of the outermost tube is fixed and that the outer tube pair is constrained to

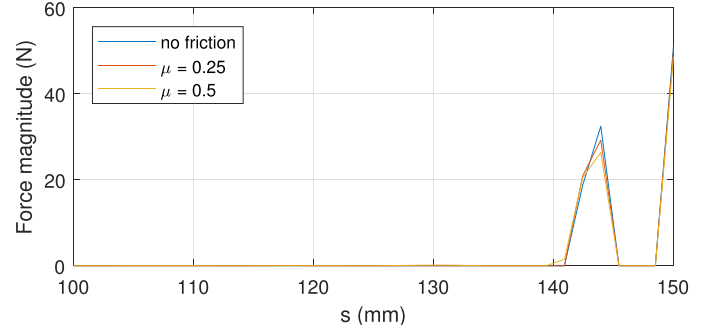


Fig. 13. Contact force magnitude versus arc length near tube tips for three values of friction coefficient and a tube clearance of 0.05 mm.

TABLE III
DIFFERENCES IN TIP POSITION BETWEEN STANDARD AND NONZERO-CLEARANCE MODELS

Model	Mean pos. diff. (mm)	Max. pos. diff. (mm)	Mean tan. diff. (°)	Max. tan. diff. (°)
Clearance	1.8(± 1.0)	4.2	2.7(± 1.2)	5.1
Friction	6.1(± 5.7)	23.8	10.7(± 9.8)	45.6

rotate, but not translate with respect to each other (creating a section of varying curvature, but fixed length), the configuration space of the three-tube robot consists of the two rotations of tube 2 and tube 3 and one translation of tube 3. A set of configurations was sampled from a $4 \times 4 \times 4$ uniform grid in the configuration space. The tip displacements induced by clearances (0.0425 mm between tubes 1 and 2; 0.0625 mm between tubes 2 and 4) and friction (friction coefficient of 0.2) were computed for these configurations. The mean and maximum differences in tip position and tangent angle for models with clearance and with clearance and friction are compared with the zero-clearance/frictionless model in Table III. One can see that the errors associated with friction are substantially larger than those associated with clearance alone. Fig. 14 depicts the configurations of maximum position difference. Note that there are four solutions of the friction model for each configuration depending on the directions of the relative tube rotations to reach the configuration. The tip positions differ significantly based on the relative rotation direction of tubes 2 and 3, but the difference is small with respect to the relative rotation direction of tubes 1 and 2.

V. PHYSICAL EXPERIMENTS

To validate the model, three experiments are reported here. The first experiment is designed to evaluate the clearance model and uses a tube pair with an optically clear outer tube to enable direct visualization of the contact regions. The second experiment investigates the effect of path history on robot configuration for a tube pair. These experiments demonstrate how large pure rotations, which are assumed by the friction model presented in Section III, produce bounding configurations. This is done by comparing solutions for path histories combining rotations and translations. The third experiment evaluates modeling error of the proposed clearance and friction models for

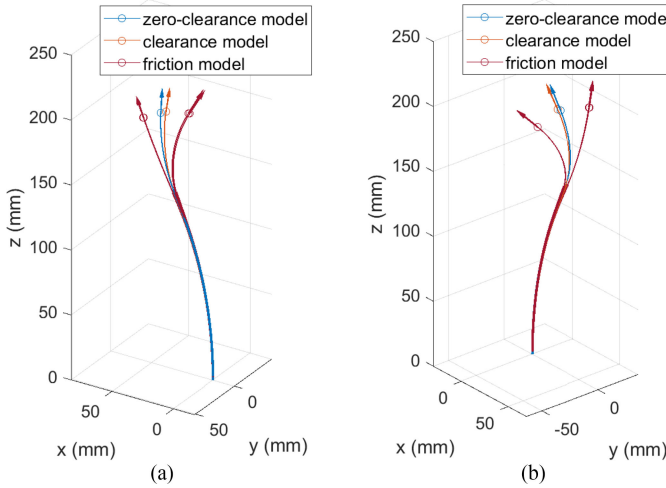


Fig. 14. Comparison between zero- and nonzero-clearance models with and without friction at configurations of maximum tip position difference between zero- and nonzero-clearance models (a) without friction and (b) with friction. The circles and the arrows indicate the tip positions and tangent vectors, respectively.

TABLE IV
PARAMETERS OF TUBE PAIR

Tube 1		Tube 2	
Section 1	Section 1	Section 1	Section 2
Length (mm)	145	17	165
Curvature (mm^{-1})	1/365	0.0	1/56
Bending Stiffness	1	0.81	
Poisson's ratio	0.48	0.3	
Clearance (mm)		1.625	

path histories consisting of large pure rotations. A three-tube robot of a size and design suitable for surgery is used in these experiments. Details of each experiment are provided in the subsections below.

A. Validation of Frictionless Clearance Model

To enable visualization of contact regions, a clear tube made of fluorinated ethylene propylene (FEP) and NiTi wire were shape set [see Fig. 15(a)] and their precurvatures and normalized (dimensionless) stiffnesses as reported in Table IV were estimated based on images of the individual tubes and the combined tubes, respectively. Only normalized tube stiffnesses are listed since the clearance model depends only on the relative stiffness of the tubes. The values of Poisson's ratio used were selected as the nominal material values. To measure the contacts with respect to arc length, the clear tube was scribed circumferentially every 3.175 mm (1/8 inches) [see Fig. 15(b)]. A line was also scribed longitudinally along the length of the tube to define a coordinate frame for each cross section. The angle of the contact region with respect to the coordinate frame was measured by sliding a paper protractor (see Fig. 16) along the tube to each contact region and measuring the angle between the longitudinal line and the contact line. The contact line between the NiTi wire and clear tube appeared as a dark line segment as shown in Fig. 15(b). The consistency of these measurements is

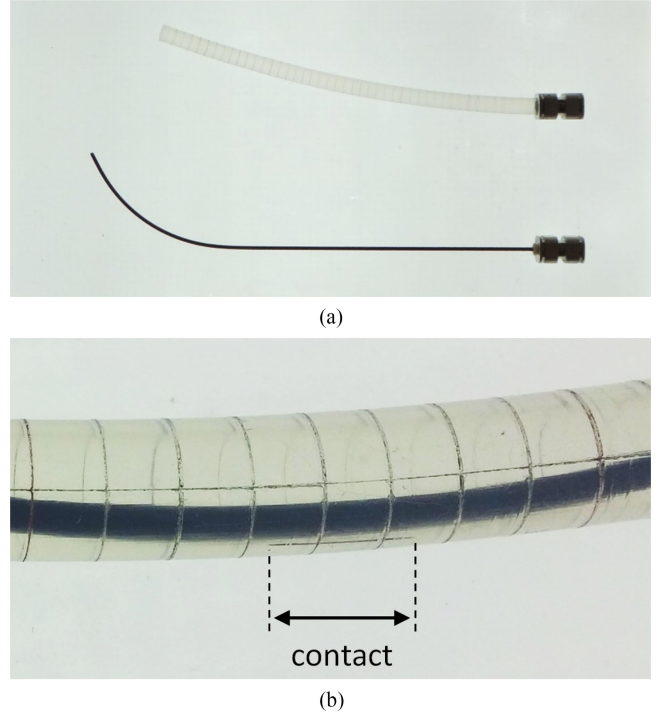


Fig. 15. Two-tube robot comprised of a clear plastic (FEP) tube and NiTi wire. (a) Robot disassembled. (b) Closeup view showing contact as dark line segment. Circumferential and longitudinal scribe marks are also shown.

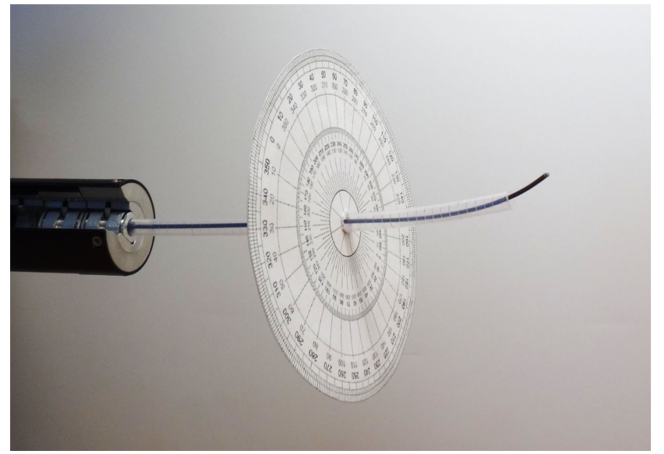


Fig. 16. Two-tube robot shown in drive system with protractor for measuring contact angles.

empirically estimated to be ± 1.5 mm in arc length and $\pm 5^\circ$ in circumferential angle.

To evaluate the clearance model by itself without considering friction or other history-dependent phenomena, an oscillatory path of decreasing amplitude was used to approach each rotational configuration [26]. The path consists of a sequence of 20 angular offsets from the desired angular configuration: $\{+40^\circ, -38^\circ, +36^\circ, \dots, -2^\circ, 0^\circ\}$. The effect of this sequence of decreasing-amplitude oscillations is to release torsional twisting due to path history.

The contact regions for seven relative angles were measured and are reported in Fig. 17. Fig. 17(a) shows the minimum

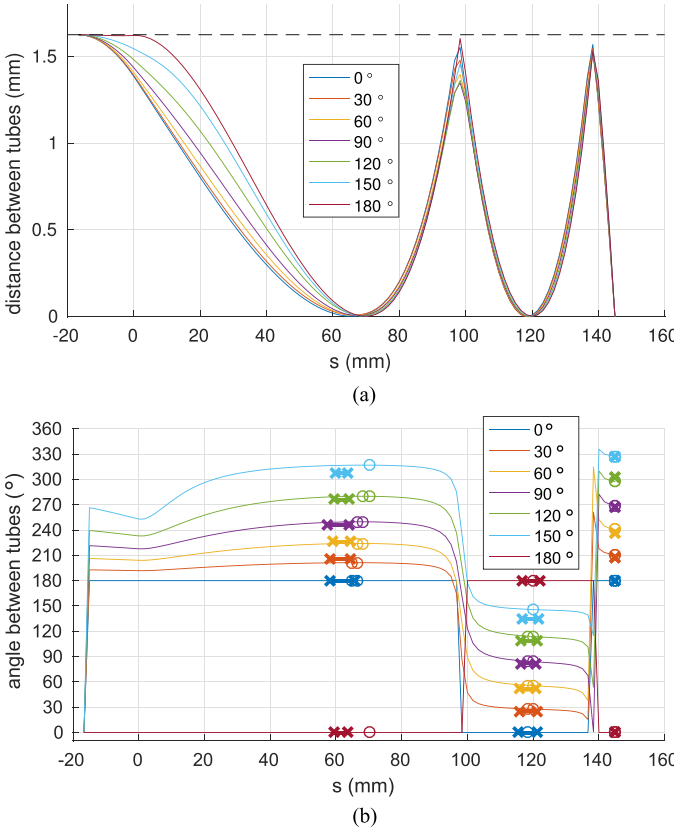


Fig. 17. Minimum directed distance between clear tube and wire. (a) Minimum radial distance. (b) Angle with respect to clear tube cross section at which minimum distance occurs. Model-predicted contacts are shown with circles. Experimentally measured contacts are shown with Xs.

distance between the wire and tube. The maximum possible distance is the clearance which is shown as a dashed line and corresponds to the intersection of the two centerlines. The three regions of contact between the wire and tube occur over the intervals for which the distance is zero. Note that the distal contact region consists of a point at the tip of the tube.

The angle of the direction of minimum distance between the tube and wire measured with respect to the tube cross section is plotted in Fig. 17(b). The predicted contact regions (zero distance) are marked by circles while the measured contact regions are denoted by line segments marked with Xs. There is good agreement between predicted and measured contact regions. For the proximal contact, the differences in contact centroid position and cross-section angle are given by 6.4 ± 1.7 mm and $3.5 \pm 3.4^{\circ}$, respectively. For the middle contact, the differences in contact centroid position and cross-section angle are given by 0.6 ± 0.3 mm and $3.7 \pm 3.8^{\circ}$, respectively. Since the third contact region is a point of contact at the tube tip, there is no difference in contact location and the difference in contact angle is given by $2.3 \pm 2.3^{\circ}$.

Recall that the zero-clearance model requires a concentrated moment to be applied to the tip of the outer tube to produce equilibrium on this cross section. This experiment reveals that the moment is actually generated by the distal pair of forces acting over a moment arm of about 26 mm.

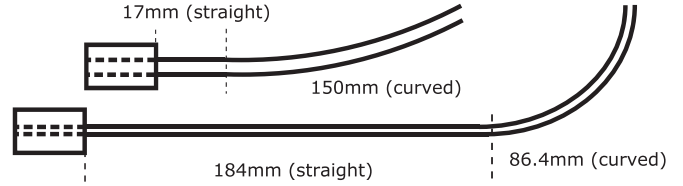


Fig. 18. Schematic of tube pair used in path history experiment.

TABLE V
PARAMETERS OF TUBE PAIR USED IN PATH HISTORY EXPERIMENT

	Tube 1		Tube 2	
	Section 1	Section 2	Section 1	Section 2
Length (mm)	17	150	184	86.4
y -curvature (mm^{-1})	0.0	$1/288.1$ ($1/265$)	0.0	$1/79.3$ ($1/55$)
x -curvature (mm^{-1})	0.0	$-1/24968.4$ (0.0)	0.0	$-1/2590.7$ (0.0)
Bending Stiffness		1		0.221 (0.286)
Poisson's ratio		0.3014 (0.3)		-0.2307 (0.3)
OD \ ID (mm)		$2.305 \setminus 1.95$		$1.875 \setminus 1.6$

B. Effect of Path History on Kinematic Configuration

The friction model presented in Section III assumes sufficient prior motion between contacting tube pairs so that the maximum Coulomb friction force is acting at each point of contact. It also assumes that this friction force is entirely directed so as to produce a twisting intertube torque. This implies that the prior motion was a pure rotation. To investigate the effect of prior rotation and translation on a tube pair, experiments were performed using the tubes shown schematically in Fig. 18 with parameters given in Table V.

The goal of the experiments was to verify that configurations reached by sufficiently large pure rotations would maximize or minimize the relative twist between the tubes compared to paths comprised of combined rotations and translations. Furthermore, one can anticipate that sufficiently large pure translations could act to reduce frictional torsional twisting so that they approach the solution predicted by the frictionless model.

Thirty-seven configurations were considered consisting of relative rotations at 10° intervals from 0° to 360° and a relative translation of 43 mm such that the curved portion of the inner tube was extended halfway from the outer tube. For each configuration, eight path histories were generated and the tip twist angle and position coordinates were recorded using electromagnetic sensors. Path histories were comprised of pure rotations (two directions), pure translations (two directions), and combined translation and rotation (four directions). Path histories were constructed by first moving to an offset configuration (90° for rotations, 10 mm for translations) and then moving to the target configuration. Rotation and translation were done simultaneously at uniform rates to linearly interpolate the offset and target configurations.

We also estimated the frictionless solution with the standard kinematics model [10] calibrated using a least squares minimization over the model parameters to minimize the sum of tip position errors, expressed as

$$\min_{\phi} \sum_{i=1}^{37 \times 8} (\|\mathbf{p}_{i,m} - \mathbf{p}_t(\phi, \mathbf{q}_i)\|)^2 \quad (48)$$

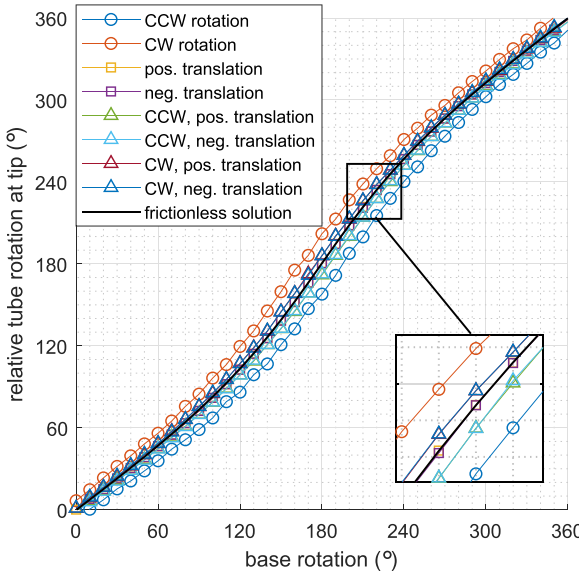


Fig. 19. Relative tube rotation angle at the tip versus base rotation angle. Measurements for eight path histories are shown for each base angle.

where ϕ and q_i are the set of calibration parameters and the configuration of the i th measurement, respectively, and $p_{i,m}$, $p_t(\phi, q_i)$ are the measured and theoretical tip positions. The model parameters were calibrated using data from all eight paths and the resulting values are also given in Table V. The bold numbers in the table are the calibrated parameters and the numbers in the parentheses are the initial values used in the calibration.

Note that the Poisson's ratio is negative for the inner tube. Recalling that the ratio of bending to torsional stiffness is given by $1 + \nu$, a negative value indicates that the stiffness ratio is smaller than anticipated. While beyond the scope of this paper, this is likely due to the higher strain in this tube leading to nonlinear behavior. In particular, the maximum strains due to bending are 0.34% for the outer tube and 1.23% for the inner tube. Only the inner tube enters the nonlinear strain region (strain $> 1\%$) and it is the only tube that experiences a negative Poisson's ratio.

Fig. 19 depicts the relative angle at the tips of the tubes as a function of base rotation angle. As anticipated the maximum and minimum twist angles for all base rotations correspond to approaching the configuration using a pure rotation. Also as expected, the two solutions corresponding to pure translations yield practically identical values of tip angle which are very close to the estimated zero-friction solution. Furthermore, the pairs of solutions combining two directions of translation with a specific direction of rotation are very close to each other and lie between the corresponding pure rotation solution and pure translation solutions.

As the tube pair is rotated through a complete revolution, the tip of the inner tube traces out an elliptical path as shown in Fig. 20. The tip paths all lie approximately on a plane rotated 23° from xy -plane about the y -axis. The maximum offset from this plane is less than 0.5 mm. The pure rotation solutions are shown as solid curves and the eight path-based configurations

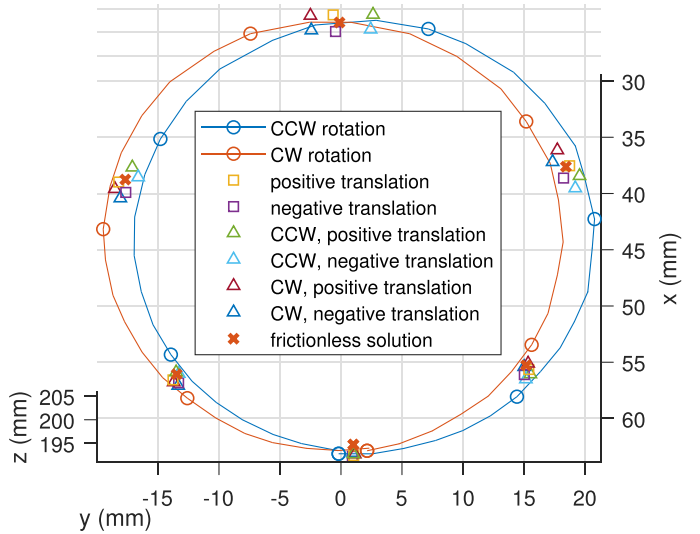


Fig. 20. Tip positions of Fig. 19. Pure-rotation path-history measurements are plotted as solid curves. The eight individual path history solutions are plotted at 60° intervals for clarity.

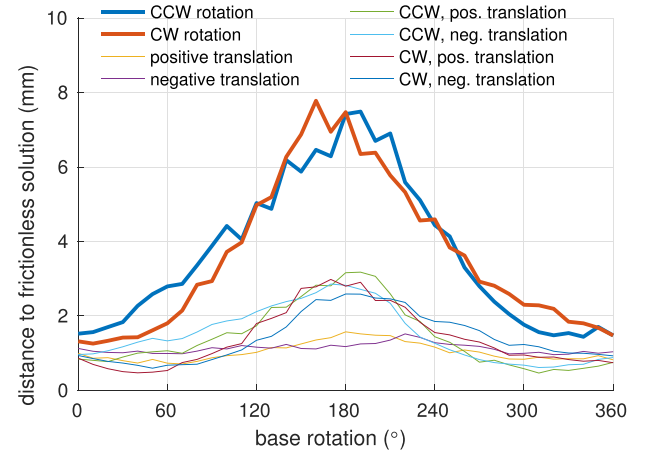


Fig. 21. Average distance of tip position from predicted frictionless solution based on path history.

are depicted for a set of six base angles. The estimated frictionless solution is also shown.

It can be observed that for each solution set, the pure rotations are farthest apart. The pure translations are located centrally, close to each other and close to the estimated frictionless solution. As in Fig. 19, the pairs of combined rotations and translations lie between the pure rotations and pure translations.

The 3-D distances between the experimental measurements and the estimated frictionless solution are plotted as a function of base rotation angle in Fig. 21. The distances are largest near a relative rotation of 180° since this is where the contact and friction forces are largest due to the precurvatures of the tubes opposing each other. This plot illustrates how pure rotation path histories produce the largest tip errors for tube pairs. The friction model proposed in this paper is intended to compute these maximum-error configurations.

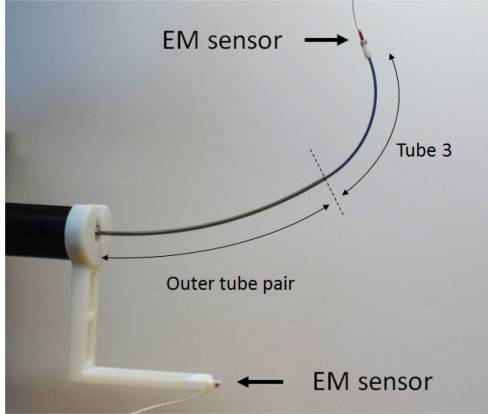


Fig. 22. Three-tube robot. EM sensors are used to measure the relative transformation from the robot base to the robot tip.

C. Validation of Friction Model

These experiments evaluate the prediction error of the friction model for path histories comprised of pure rotations. Its performance is compared to the standard frictionless model [10] as well as to the frictionless clearance model. The three-tube robot shown in Fig. 22 was used and a 6-DOF electromagnetic (EM) sensor (Model 180, Ascension Technologies) recorded tip position and orientation. Sensor position and orientation accuracies are 1.4 mm rms and 0.5° rms. We performed our experiments in the region with the best measurement quality indicated by the manufacturer's software and averaged measurements over 2 s (about 200 measurements) to clear our high-frequency noise. Ignoring rigid-body motions, the robot degrees of freedom consist of the two relative rotations of the three tubes and the relative translation of the distal tube with respect to the proximal pair (the proximal pair of tubes are designed to translate together). The nominal tube parameters are given in Table II.

Since each robot configuration is described by two relative angles, a specific configuration can be approached from four angular “directions.” The four angular directions correspond to the following rotation directions of the second and third tubes relative to the first and second tubes, respectively: (1) CCW, CCW, (2) CCW, CW, (3) CW, CCW, and (4) CW, CW. Each of the relative rotations is performed by 90° of tube base rotation, which was found to be sufficient to produce the maximum torsional friction effect. An example configuration is depicted in Fig. 23, in which path direction produced four different tip positions that differ from each other by up to 17 mm.

Tip position and tangent direction were collected for each of the four approach directions at $8 \times 8 \times 8$ configurations evenly distributed in joint space. This dataset was divided into two subsets. The first, comprising 62 configurations ($\times 4$ angular directions), was used for calibration while the remaining 450 configurations ($\times 4$ angular directions) were used for error computation. The 62 configurations were selected as $4 \times 4 \times 4$ subset configurations evenly distributed in the joint space. Two configurations in the set of $4 \times 4 \times 4$ were excluded since they were predicted to possess multiple solutions using the standard zero-clearance model with the nominal parameters.

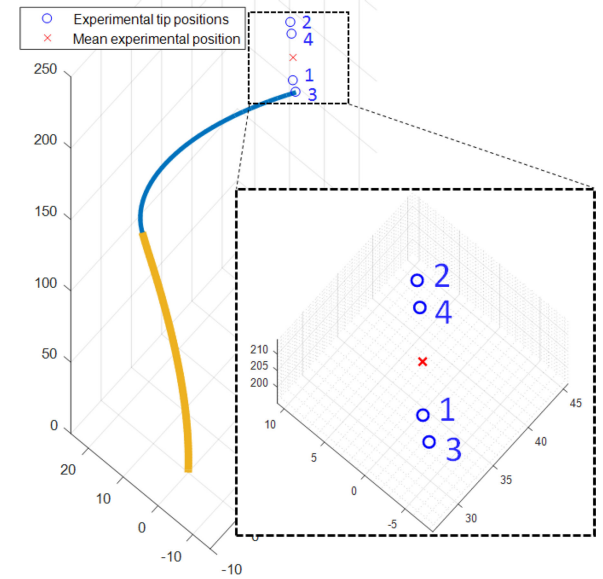


Fig. 23. Example showing four experimentally measured robot tip positions corresponding to the four rotational paths of a single set of base angles.

TABLE VI
STANDARD FRICTIONLESS MODEL PARAMETERS

	Tube 1		Tube 2		Tube 3	
	Section 1	Section 2	Section 1	Section 2	Section 1	Section 2
Length (mm)	150	17	150	184	86.4	
<i>y</i> -curvature (mm ⁻¹)	1/276.5	0.0	1/212.4	0.0	1/61.01	
<i>x</i> -curvature (m ⁻¹)	-1/1775.0	0.0	-1/9.791	0.0	-1/3.526	
Bending Stiffness	1		1.006		0.2742	
Poisson's ratio	0.3208		0.3415		-0.1750	

Estimated parameters are bolded.

Model calibration was performed as a least squares minimization over the model parameters. For these experiments, we minimized the weighted sum of tip position and tangent errors, expressed as

$$\min_{\phi} \sum_{i=1}^{62 \times 4} \left(\| \mathbf{p}_{i,m} - \mathbf{p}_t(\phi, \mathbf{q}_i) \| + \frac{180}{\pi} \cos^{-1} (\mathbf{t}_{i,m} \cdot \mathbf{t}_t(\phi, \mathbf{q}_i)) \right)^2 \quad (49)$$

where ϕ and \mathbf{q}_i are the set of calibration parameters and the configuration of i th measurement, respectively, and $\mathbf{p}_{i,m}$, $\mathbf{p}_t(\phi, \mathbf{q}_i)$, $\mathbf{t}_{i,m}$ and $\mathbf{t}_t(\phi, \mathbf{q}_i)$ are the measured and the theoretical tip positions and the measured and theoretical tip tangents, respectively. This choice of weighting function scales 1° of tangent error to be equal to 1mm of position error.

The calibrated tube parameters for the standard frictionless model are given in Table VI and those of the frictionless clearance model and the friction model are given in Table VII. Only the normalized tube stiffnesses are listed since the model depends only on the relative stiffness of the tubes. In the clearance model and the friction model, the tube-to-tube clearances are not calibrated but given by the nominal inner and outer diameters of the tubes. The bolded numbers in the tables are the parameters that have been calibrated while the others were fixed in the calibration. Parameters were calibrated through a gradient descent method. The friction coefficients were calibrated during

TABLE VII
PARAMETERS OF FRICTIONLESS CLEARANCE AND FRICTION MODELS

	Tube 1		Tube 2		Tube 3	
Section 1	Section 1	Section 2	Section 1	Section 2	Section 1	Section 2
Length (mm)	150	17	150	184	86.4	
<i>y</i> -curvature (mm ⁻¹)	1/282.8	0.0	1/212.6	0.0	1/62.37	
<i>x</i> -curvature (m ⁻¹)	-1/291.3	0.0	-1/9.879	0.0	-1/3.313	
Bending Stiffness	1		0.9929		0.1990	
Poisson's ratio	0.3000		0.3256		-0.1543	
Outer diameter	2.64		2.31		1.83	
Clearance (mm)	0.0425		0.0625			
Friction coefficient	0.22		0.12			

Estimated parameters are bolded.

TABLE VIII
MODELING ERROR OF CALIBRATED STANDARD, CLEARANCE, AND FRICTION MODELS

Model	Mean pos. error (mm)	Max. pos. error (mm)	Mean tan. error (°)	Max. tan. error (°)	Evaluation time (sec)
Standard	4.1(± 2.3)	11.5	4.9(± 2.7)	14.3	0.23(± 0.10)
Clearance	3.7(± 2.1)	11.6	4.9(± 2.7)	14.9	5.3(± 2.2)
Friction	2.2(± 0.9)	5.9	1.8(± 0.9)	7.1	11.7(± 4.4)

a second pass using a 2-D grid search to avoid local minima. This approach allows the frictionless clearance model and the friction model to share the same tube parameters. Furthermore, calibration performed over all parameters simultaneously was performed and did not improve the model fit.

Note that while the tube precurvatures were in the *y*-direction, the calibration allowed nonzero curvatures in the *x*-direction. In other words, the *y*-curvature is the main tube precurvature and the *x*-curvature is off-plane curvature that can be produced unintentionally during the manufacturing process. The *x*-curvature is at least 46 times smaller than the *y*-curvature in Tables VI and VII.

Also, notice that the calibrated values for Poisson's ratio of the innermost tube for all models are negative. As described in the tube pair example above, this is likely due to the higher strains in this tube leading to nonlinear behavior. In particular, the maximum strains due to tube bending are computed to be 0.73%, 0.65%, and 1.68% for tubes 1 to 3, respectively, using the tube parameters in Table VII. Only tube 3 enters the nonlinear strain region (strain > 1%) and it is the only tube that experiences a negative Poisson's ratio.

The mean and maximum errors in tip position and tangent direction for the three models were computed using the 450 robot configurations ($\times 4$ angular directions) collected as described earlier. The results are reported in Table VIII along with the CPU evaluation time for each model. All models were coded in MATLAB and running on a PC equipped with Intel(R) Core(TM) i5-3470 CPU. Since the frictionless standard and clearance models produce a single solution for each robot configuration, the inclusion of all four angular-directions measurements in both the calibration and evaluation steps is similar to employing the “average” tip position and tangent direction for each configuration [26].

There is no statistically significant difference between the mean prediction errors of the frictionless standard and clearance models and the maximum errors are also similar. Note that the two models have the same number of parameters. While not

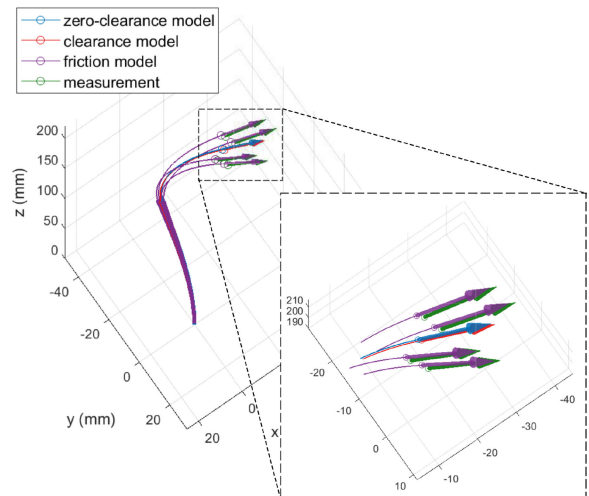


Fig. 24. Example configuration comparing four experimental solutions with the single predictions of the standard and clearance models and the four solutions of the friction model. Circles denote tip positions and semitransparent arrows indicate tip tangent vectors.

included here, we also fit the clearance model while allowing the clearance parameters to vary. These additional parameters had little effect on the average and maximum errors.

In contrast, the friction model provides a significant improvement over the other two models. The error mean and standard deviation are reduced in both tip position and tangent direction. Perhaps the most important reduction is that the maximum errors in position and tangent direction are reduced by 48% and 50%, respectively. Note, however, that, as implemented, the friction model takes 51 times as long to evaluate.

A comparison of models at a typical configuration is shown in Fig. 24. The friction model produces four solutions according to the angular directions by which the configuration is approached. These solutions can be seen to approximate the four corresponding experimental measurements. The frictionless models each produce a single solution that, to some extent, models the “mean” of the four solutions.

VI. CONCLUSION

This paper has demonstrated how tube clearance and torsional Coulomb friction can be incorporated in the existing mechanics-based but approximate kinematic model. The clearance model by itself does not reduce modeling error, but is a necessary step for computing friction torques based on the contact forces between tubes. It also reveals some interesting details about tube interaction. For example, the concentrated moment that the standard model assumes at the end of each tube (except the most distal one) was found to be comprising a distributed force and point force acting as a force couple over a centimeter-scale distance.

The friction model, as formulated, assumes that the maximum Coulomb force is generated along the entire interface between each contacting pair of tubes and is directed circumferentially. This produces solutions in which friction either maximizes or minimizes the twisting between each pair of contacting

tubes and corresponds to purely rotational path histories. It was demonstrated experimentally for a tube pair that purely rotational path histories produce the maximum tip error compared to translations or mixed translations and rotations. Consequently, the friction model provides worst case estimates of actual tip configurations for arbitrary path histories.

Additional experiments revealed that, for path histories of pure rotation, the friction model produced a significant reduction in average error. Maximum error was also reduced by half when compared to the standard kinematic model. The price paid for improved modeling accuracy was a substantial increase in model computation time.

While such a model is not appropriate for real-time feedback control, it is valuable for path planning since it can be used to estimate the maximum path-dependent errors for a specific robot configuration. Furthermore, knowledge of how path history (rotations versus translations) affects friction-induced tube twisting can also guide path planning. For example, set-point interpolation can be designed to favor performing translations after rotations in order to reduce torsional friction.

APPENDIX A

EFFICIENT COMPUTATION OF $\Delta\vec{u} = \mathbf{Q}^{-1}\mathbf{h}$

An efficient way of computing $\Delta\vec{u} = \mathbf{Q}^{-1}\mathbf{h}$ is presented here. Consider \mathbf{Q} given in (28) for the frictionless case and in (45) for the case with friction. The derivation here focuses on (45) since (28) is a special case of (45) with zero friction coefficients, i.e., $\mu_k = 0$. The matrix \mathbf{Q} in (45) can be expressed without \sum as

$$\mathbf{Q}(\lambda) = \mathbf{K} + \mathbf{Y}^T \boldsymbol{\Lambda} \mathbf{X} \quad (50)$$

with

$$\mathbf{X} = [\mathbf{X}_{k_1}^T \mathbf{X}_{k_2}^T \dots]^T \in \mathbb{R}^{3m \times 3N} \quad (51)$$

$$\mathbf{Y} = [\mathbf{Y}_{k_1}^T \mathbf{Y}_{k_2}^T \dots]^T \in \mathbb{R}^{3m \times 3N} \quad (52)$$

$$\boldsymbol{\Lambda} = \begin{bmatrix} \lambda_{k_1} \mathbf{I}_{3 \times 3} & & 0 \\ & \lambda_{k_2} \mathbf{I}_{3 \times 3} & \\ 0 & & \ddots \end{bmatrix} \in \mathbb{R}^{3m \times 3m} \quad (53)$$

where k_1, k_2, \dots, k_m are the indices of nonzero λ_k . Applying the Woodbury matrix identity [27], $\mathbf{Q}^{-1}\mathbf{h}$ is given by

$$\mathbf{Q}^{-1}\mathbf{h} = \mathbf{K}^{-1}\mathbf{h} - \mathbf{K}^{-1}\mathbf{Y}^T (\boldsymbol{\Lambda}^{-1} + \mathbf{X}\mathbf{K}^{-1}\mathbf{Y}^T)^{-1} \mathbf{X}\mathbf{K}^{-1}\mathbf{h}. \quad (54)$$

Here, the diagonal matrices \mathbf{K} and $\boldsymbol{\Lambda}$ can be efficiently inverted by component-wise inversions. The other matrix to invert, $\boldsymbol{\Lambda}^{-1} + \mathbf{X}\mathbf{K}^{-1}\mathbf{Y}^T$, is a $3m \times 3m$ matrix where m is the number of nonzero λ_k . The dimension of this matrix is smaller than that of $\mathbf{Q} (\in \mathbb{R}^{3N \times 3N})$. Thus, the computation involved in the matrix inversion is more efficient, especially when λ is nearly converged since λ_k in the converged solution are mostly zero, i.e., the contact forces are mostly zero along the length, as shown in Figs. 10, 12, and 17.

For more efficient computation, $(\boldsymbol{\Lambda}^{-1} + \mathbf{X}\mathbf{K}^{-1}\mathbf{Y}^T)^{-1} \mathbf{X}\mathbf{K}^{-1}\mathbf{h}$ can be set equal to \mathbf{v} and computed through solving the linear

equation below for the unknown \mathbf{v} :

$$(\boldsymbol{\Lambda}^{-1} + \mathbf{X}\mathbf{K}^{-1}\mathbf{Y}^T)\mathbf{v} = \mathbf{X}\mathbf{K}^{-1}\mathbf{h}. \quad (55)$$

Then $\Delta\vec{u}$ is computed by substituting \mathbf{v} in

$$\Delta\vec{u} = \mathbf{K}^{-1}\mathbf{h} - \mathbf{K}^{-1}\mathbf{Y}^T \mathbf{v}. \quad (56)$$

In summary, the equation $\Delta\vec{u} = \mathbf{Q}^{-1}\mathbf{h}$ can be efficiently solved for $\Delta\vec{u}$ by first solving (55) for \mathbf{v} and substituting the resulting \mathbf{v} into (56).

APPENDIX B ANALYTIC FORMS OF \mathbf{J}_p AND \mathbf{J}_ω

The Jacobian matrix $\mathbf{J}_p \in \mathbb{R}^{3N \times 3N}$ is the linear map between changes in tube curvatures and changes in tube centerlines around the initial solution $\{\mathbf{u}_i^*(s), \mathbf{R}_i^*(s), \mathbf{p}_i^*(s)\}_{i=1,\dots,n}$. Similarly, $\mathbf{J}_\omega \in \mathbb{R}^{3N \times 3N}$ maps the changes in tube curvatures to the angular displacements of the tube frames $\{\mathbf{R}_i(s)\}_{i=1,\dots,n}$. The analytic forms of these matrices are derived here. The formulation of \mathbf{J}_p is more accurate than (26) in [16] as it accurately incorporates tube curvature between discretized points.

As the tube lengths are discretized, the Jacobian matrices depend on the numerical integration of the centerlines and the frames along the tubes. While any numerical integration can be chosen, the analytic forms of \mathbf{J}_p and \mathbf{J}_ω to be derived here are based on Euler integration in the exponential coordinate of $SE(3)$, shown as follows:

$$\mathbf{T}_i(s + \Delta s) = \mathbf{T}_i(s) \exp \left(\begin{bmatrix} \langle \mathbf{u}_i(s) \rangle & \hat{\mathbf{e}}_z \\ \mathbf{0}_{1 \times 3} & 0 \end{bmatrix} \Delta s \right) \quad (57)$$

where Δs is the arc length step, $\hat{\mathbf{e}}_z = [0 \ 0 \ 1]^T$ is the unit vector along the z -axis, and $\mathbf{T}_i(s) \in SE(3)$ is the 4×4 transformation matrix that represents the body frame and the position of tube i at s , which is of the form

$$\mathbf{T}_i(s) = \begin{bmatrix} \mathbf{R}_i(s) & \mathbf{p}_i(s) \\ \mathbf{0}_{1 \times 3} & 1 \end{bmatrix}. \quad (58)$$

Defining $\mathbf{J}_{p,i} \in \mathbb{R}^{3N_i \times 3N_i}$ and $\mathbf{J}_{\omega,i} \in \mathbb{R}^{3N_i \times 3N_i}$ as the Jacobian matrices for tube i only, they align diagonally in \mathbf{J}_p and \mathbf{J}_ω of the form

$$\mathbf{J}_p = \begin{bmatrix} \mathbf{J}_{p,1} & & 0 \\ & \ddots & \\ 0 & & \mathbf{J}_{p,n} \end{bmatrix}, \quad \mathbf{J}_\omega = \begin{bmatrix} \mathbf{J}_{\omega,1} & & 0 \\ & \ddots & \\ 0 & & \mathbf{J}_{\omega,n} \end{bmatrix}. \quad (59)$$

By decomposing $\mathbf{J}_{p,i}$ and $\mathbf{J}_{\omega,i}$ further into 3×3 blocks, their (j, k) th 3×3 blocks can be expressed, respectively, as

$$\mathbf{J}_{p,i}(j, k) = \frac{\partial \mathbf{p}_i(s_{ij})}{\partial \mathbf{u}_i(s_{ik})} \in \mathbb{R}^{3 \times 3} \quad (60)$$

$$\mathbf{J}_{\omega,i}(j, k) = \frac{\partial \boldsymbol{\omega}_i(s_{ij})}{\partial \mathbf{u}_i(s_{ik})} \in \mathbb{R}^{3 \times 3} \quad (61)$$

which represent the linear maps between small changes in the curvature at k th point on tube i and corresponding changes in $\mathbf{p}_i(s)$ and $\boldsymbol{\omega}_i(s)$ at j th point on tube i . Here $\boldsymbol{\omega}_i(s) \in \mathbb{R}^3$ is the angular displacement of $\mathbf{R}_i(s)$ from $\mathbf{R}_i^*(s)$, i.e., $\mathbf{R}_i(s) = \mathbf{R}_i^*(s) \exp(\langle \boldsymbol{\omega}_i(s) \rangle)$.

To derive $\mathbf{J}_{p,i}(j, k)$ and $\mathbf{J}_{\omega,i}(j, k)$, we will express the relations of $\mathbf{p}_i(s_{ij})$, $\boldsymbol{\omega}_i(s_{ij})$, and $\mathbf{u}_i(s_{ik})$ as a matrix equation and expand this as the first-order Taylor series. This results in a set of linear equations that represent linear maps between small changes of $(\mathbf{p}_i(s_{ij}), \boldsymbol{\omega}_i(s_{ij}), \mathbf{u}_i(s_{ik}))$, where the linear maps correspond to the matrices $\mathbf{J}_{p,i}(j, k)$ and $\mathbf{J}_{\omega,i}(j, k)$. Note that $\mathbf{J}_{p,i}(j, k)$ and $\mathbf{J}_{\omega,i}(j, k)$ for $j < k$ are zero matrices as the curvature change at a point doesn't influence \mathbf{p}_i or $\boldsymbol{\omega}_i$ at more proximal points. The following derivations will thus focus on $j \geq k$.

Let us begin with the following obvious equation:

$$\mathbf{T}_i(s_{ij}) = \mathbf{T}_i(s_{ik}) \mathbf{T}_i^{-1}(s_{ik}) \mathbf{T}_i(s_{i(k-1)}) \mathbf{T}_i^{-1}(s_{i(k-1)}) \mathbf{T}_i(s_{ij}). \quad (62)$$

To have $\mathbf{u}_i(s_{jk})$ appear in the equation, $\mathbf{T}_i^{-1}(s_{ik}) \mathbf{T}_i(s_{i(k-1)})$ will be substituted with an exponential map associated with $\mathbf{u}_i(s_{jk})$, as follows:

$$\mathbf{T}_i(s_{ij}) = \mathbf{T}_i(s_{ik}) \exp(\mathbf{V} \Delta s) \mathbf{T}_i^{-1}(s_{i(k-1)}) \mathbf{T}_i(s_{ij}) \quad (63)$$

where

$$\mathbf{V} = \begin{bmatrix} \langle \mathbf{u}_i(s_{jk}) \rangle & \hat{\mathbf{e}}_z \\ \mathbf{0}_{1 \times 3} & 0 \end{bmatrix} \in \mathbb{R}^{4 \times 4}. \quad (64)$$

Note that (63) relates $\mathbf{p}_i(s_{ij})$, $\boldsymbol{\omega}_i(s_{ij})$, and $\mathbf{u}_i(s_{ik})$ as $\mathbf{T}_i(s_{ij})$ is a function of $\mathbf{p}_i(s_{ij})$ and $\boldsymbol{\omega}_i(s_{ij})$, i.e.,

$$\mathbf{T}_i(s_{ij}) = \begin{bmatrix} \mathbf{R}_i^*(s_{ij}) \exp(\langle \boldsymbol{\omega}_i(s_{ij}) \rangle) & \mathbf{p}_i(s_{ij}) \\ \mathbf{0}_{1 \times 3} & 1 \end{bmatrix}. \quad (65)$$

The first-order Taylor expansion of (63) with respect to $(\mathbf{p}_i(s_{ij}), \boldsymbol{\omega}_i(s_{ij}), \mathbf{u}_i(s_{ik}))$ about the initial solution $(\mathbf{u}_i^*(s), \mathbf{R}_i^*(s), \mathbf{p}_i^*(s))$ is given by

$$\begin{bmatrix} \mathbf{R}_i^*(s_{ij}) \langle \delta \boldsymbol{\omega}_i(s_{ij}) \rangle & \delta \mathbf{p}_i(s_{ij}) \\ \mathbf{0}_{1 \times 3} & 0 \end{bmatrix} = \mathbf{T}_i^*(s_{ik}) \text{dexp}_{(\mathbf{V}^* \Delta s)} (\delta \mathbf{u}(s_{ik}) \Delta s) \mathbf{T}_i^{*-1}(s_{i,k}) \mathbf{T}_i^*(s_{i,j}) \quad (66)$$

where \mathbf{V}^* is defined by substituting $\mathbf{u}_i(s_{ik})$ in (64) with $\mathbf{u}_i^*(s_{ik})$. Here $\text{dexp}_{(\cdot)}$ denotes the differential of the exponential map [28] and the variables with δ represent the small changes of the corresponding variables. After an algebraic manipulation, (66) reduces to the following linear equations:

$$\delta \mathbf{p}_i(s_{ij}) = \mathbf{J}_{p,i}(j, k) \delta \mathbf{u}_i(s_{ik}) \quad (67)$$

$$\delta \boldsymbol{\omega}_i(s_{ij}) = \mathbf{J}_{\omega,i}(j, k) \delta \mathbf{u}_i(s_{ik}) \quad (68)$$

where the matrices $\mathbf{J}_{p,i}(j, k)$ and $\mathbf{J}_{\omega,i}(j, k)$ can be expressed using the differential of the exponential map. Based on the formulations of the differential of the exponential map in [28], $\mathbf{J}_{p,i}(j, k)$ and $\mathbf{J}_{\omega,i}(j, k)$ are given by

$$\mathbf{J}_{p,i}(j, k) = \langle \mathbf{p}_i^*(s_{ij}) - \mathbf{p}_i^*(s_{ik}) \rangle \mathbf{D}_{ik} + \mathbf{E}_{ik} \quad (69)$$

$$\mathbf{J}_{\omega,i}(j, k) = \mathbf{R}_i^{*T}(s_{ij}) \mathbf{D}_{ik} \quad (70)$$

with $\mathbf{D} \in \mathbb{R}^{3 \times 3}$ and $\mathbf{E} \in \mathbb{R}^{3 \times 3}$ defined as

$$\mathbf{D}_{ik} = \mathbf{R}_i^*(s_{ik}) \left(\text{dexp}_{\mathbf{u}_i^*(s_{ik}) \Delta s} \right) \Delta s \quad (71)$$

$$\mathbf{E}_{ik} = \mathbf{R}_i^*(s_{ik}) \left(C(\mathbf{u}_i^*(s_{ik}) \Delta s) + \frac{1}{2} \langle \hat{\mathbf{e}}_z \rangle \right) \Delta s \quad (72)$$

where the 3×3 matrices $\text{dexp}_{(\cdot)}$ and $C(\cdot)$ are given in [28] by

$$\text{dexp}_{\mathbf{u}} = \mathbf{I}_{3 \times 3} + \frac{1}{2} \beta \langle \mathbf{u} \rangle + \frac{1 - \alpha}{\|\mathbf{u}\|^2} \langle \mathbf{u} \rangle^2 \quad (73)$$

$$\begin{aligned} C(\mathbf{u}) = & -\frac{1 - \beta}{2} \langle \hat{\mathbf{e}}_z \rangle + \frac{1 - \alpha}{\|\mathbf{u}\|^2} (\langle \hat{\mathbf{e}}_z \rangle \langle \mathbf{u} \rangle + \langle \mathbf{u} \rangle \langle \hat{\mathbf{e}}_z \rangle) \\ & + \frac{\alpha - \beta}{\|\mathbf{u}\|^2} (\mathbf{u}^T \hat{\mathbf{e}}_z) \langle \mathbf{u} \rangle \\ & + \frac{1}{\|\mathbf{u}\|^2} \left(\frac{1}{2} \beta - \frac{3}{\|\mathbf{u}\|^2} (1 - \alpha) \right) (\mathbf{u}^T \hat{\mathbf{e}}_z) \langle \mathbf{u} \rangle^2 \end{aligned} \quad (74)$$

and α and β are given by

$$\alpha = \frac{2 \sin \frac{\|\mathbf{u}\|}{2} \cos \frac{\|\mathbf{u}\|}{2}}{\|\mathbf{u}\|}, \quad \beta = \frac{4 \sin^2 \frac{\|\mathbf{u}\|}{2}}{\|\mathbf{u}\|^2}. \quad (75)$$

In summary, the overall computation is as follows:

- 1) For tube i , compute $\mathbf{J}_{p,i}(j, k)$ and $\mathbf{J}_{\omega,i}(j, k)$ over $j = 1, \dots, N_i$ and $k = 1, \dots, N_i$ using (69)–(75). Remember that $\mathbf{J}_{p,i}(j, k) = \mathbf{J}_{\omega,i}(j, k) = \mathbf{0}_{3 \times 3}$ for $j < k$.
- 2) Build $\mathbf{J}_{p,i}$ and $J_{\omega,i}$ by collecting $\mathbf{J}_{p,i}(j, k)$ and $J_{\omega,i}(j, k)$ as (j, k) th 3×3 blocks.
- 3) Repeat (1) and (2) for all tubes and build \mathbf{J}_p and \mathbf{J}_ω using (59).

REFERENCES

- [1] N. V. Vasilyev, P. E. Dupont, and P. J. Del Nido, "Robotics and imaging in congenital heart surgery," *Future Cardiology*, vol. 8, no. 2, pp. 285–296, 2012.
- [2] A. H. Gosline *et al.*, "Percutaneous intracardiac beating-heart surgery using metal MEMS tissue approximation tools," *Int. J. Robot. Res.*, vol. 31, no. 9, pp. 1081–1093, 2012.
- [3] N. V. Vasilyev *et al.*, "Percutaneous steerable robotic tool delivery platform and metal MEMS device for tissue manipulation and approximation: Initial experience with closure of patent foramen ovale," *Circulation: Cardiovascular Interventions*, vol. 6, pp. 468–475, 2013.
- [4] N. V. Vasilyev *et al.*, "Tissue removal inside the beating heart using a robotically delivered metal MEMS tool," *Int. J. Robot. Res.*, vol. 34, no. 2, pp. 236–247, 2015.
- [5] J. Burgner *et al.*, "A telerobotic system for transnasal surgery," *IEEE/ASME Trans. Mechatronics*, vol. 19, no. 3, pp. 996–1006, Jun. 2014.
- [6] T. Anor, J. R. Madsen, and P. Dupont, "Algorithms for design of continuum robots using the concentric tubes approach: A neurosurgical example," in *Proc. IEEE Int. Conf. Robot. Automat.*, 2011, pp. 667–673.
- [7] L. A. Lyons, R. J. Webster III, and R. Alterovitz, "Motion planning for active cannulas," *Proc. IEEE/RSJ Int. Conf. Intell. Robots Syst.*, 2009, pp. 801–806.
- [8] L. Lyons, R. W. III, and R. Alterovitz, "Planning active cannula configurations through tubular anatomy," *Proc. IEEE Int. Conf. Robot. Automat.*, 2010, pp. 2082–2087.
- [9] L. G. Torres, R. J. Webster III, and R. Alterovitz, "Task-oriented design of concentric tube robots using mechanics-based models," *Proc. IEEE/RSJ Int. Conf. Intell. Robots Syst.*, 2012, pp. 4449–4455.
- [10] P. E. Dupont, J. Lock, B. Itkowitz, and E. Butler, "Design and control of concentric tube robots," *IEEE Trans. Robot.*, vol. 26, no. 2, pp. 209–225, Apr. 2010.
- [11] D. C. Rucker, B. A. Jones, and R. J. Webster III, "A geometrically exact model for externally-loaded concentric-tube continuum robots," *IEEE Trans. Robot.*, vol. 26, no. 5, pp. 769–780, Oct. 2010.

- [12] D. C. Rucker, R. J. Webster, G. S. Chirikjian, and N. J. Cowan, "Equilibrium conformations of concentric-tube continuum robots," *Int. J. Robot. Res.*, vol. 29, no. 10, pp. 1263–1280, 2010.
- [13] J. Ha, F. C. Park, and P. E. Dupont, "Elastic stability of concentric tube robots subject to external loads," *IEEE Trans. Biomed. Eng.*, vol. 63, no. 6, pp. 1116–1128, Jun. 2016.
- [14] J. Lock and P. E. Dupont, "Friction modeling in concentric tube robots," in *Proc. IEEE Int. Conf. Robot. Automat.*, 2011, pp. 1139–1146.
- [15] B. Armstrong-Hélouvry, P. E. Dupont, and C. C. De Wit, "A survey of models, analysis tools and compensation methods for the control of machines with friction," *Automatica*, vol. 30, no. 7, pp. 1083–1138, 1994.
- [16] J. Ha and P. E. Dupont, "Incorporating tube-to-tube clearances in the kinematics of concentric tube robots," in *Proc. IEEE Int. Conf. Robot. Automat.*, 2017, pp. 6730–6736.
- [17] O. A. Bauchau and C. Ju, "Modeling friction phenomena in flexible multi-body dynamics," *Comput. Methods Appl. Mech. Eng.*, vol. 195, no. 50–51, pp. 6909–6924, 2006.
- [18] K. B. Reed, A. M. Okamura, and N. J. Cowan, "Modeling and control of needles with torsional friction," *IEEE Trans. Biomed. Eng.*, vol. 56, no. 12, pp. 2905–2916, Dec. 2009.
- [19] S. J. Phee, S. Low, P. Dario, and A. Menciassi, "Tendon sheath analysis for estimation of distal end force and elongation for sensorless distal end," *Robotica*, vol. 28, no. 7, pp. 1073–1082, 2010.
- [20] V. Agrawal, W. J. Peine, and B. Yao, "Modeling of transmission characteristics across a cable-conduit system," *IEEE Trans. Robot.*, vol. 26, no. 5, pp. 914–924, Oct. 2010.
- [21] T. Kato, I. Okumura, S.-E. Song, A. J. Golby, and N. Hata, "Tendon-driven continuum robot for endoscopic surgery: preclinical development and validation of a tension Propagation model," *IEEE/ASME Trans. Mechatronics*, vol. 20, no. 5, pp. 2252–2263, Oct. 2015.
- [22] R. Roy, L. Wang, and N. Simaan, "Modeling and estimation of friction, extension, and coupling effects in multisegment continuum robots," *IEEE/ASME Trans. Mechatronics*, vol. 22, no. 2, pp. 909–920, Apr. 2017.
- [23] S. Boyd and L. Vandenberghe, *Convex Optimization*. Cambridge, U.K.: Cambridge Univ. Press, 2004.
- [24] B. Siciliano, L. Sciavicco, L. Villani, and G. Oriolo, *Robotics: Modelling, Planning and Control*. London, U.K.: Springer-Verlag, 2010.
- [25] J. Ha, F. C. Park, and P. E. Dupont, "Optimizing tube precurvature to enhance elastic stability of concentric tube robots," *IEEE Trans. Robot.*, vol. 33, no. 1, pp. 22–37, Feb. 2017.
- [26] J. Ha, G. Fagogenis, and P. E. Dupont, "Effect of path history on concentric tube robot model calibration," in *Proc. 10th Hamlyn Symp. Med. Robot.*, 2017, pp. 77–78.
- [27] M. A. Woodbury, "Inverting modified matrices," *Memorandum Rep.*, vol. 42, no. 106, p. 336, 1950.
- [28] J. Park and W.-K. Chung, "Geometric integration on Euclidean group with application to articulated multibody systems," *IEEE Trans. Robot.*, vol. 21, no. 5, pp. 850–863, 2005.



Junhyoung Ha received the B.S. and Ph.D. degrees in mechanical engineering from Seoul National University, Seoul, South Korea, in 2008 and 2015, respectively.

He is currently a Postdoctoral Fellow with Boston Children's Hospital, Harvard Medical School, Boston, MA, USA. His research interests include medical robotics, continuum robots, control, and optimization.



Georgios Fagogenis received the diploma in mechanical engineering from the National Technical University of Athens, Athens, Greece, in 2007, the M.S. degree in mechanical engineering from ETH Zurich, Zurich, Switzerland, in 2009, and the Ph.D. degree in electrical engineering from Heriot-Watt University, Edinburgh, Scotland, in 2016.

He is currently a Postdoctoral Fellow with Boston Children's Hospital, Harvard Medical School, Boston, MA, USA. His research interests include medical robotics and autonomous surgery.



Pierre E. Dupont (M'99–SM'03–F'11) received the B.S., M.S., and Ph.D. degrees in mechanical engineering from Rensselaer Polytechnic Institute, Troy, NY, USA, in 1982, 1984, and 1988, respectively.

From 1988 to 1990, he was a Postdoctoral Fellow with the School of Engineering and Applied Sciences, Harvard University, Cambridge, MA, USA. He was a Professor of mechanical engineering and biomedical engineering with Boston University, Boston, MA, USA. He is currently the Chief of Pediatric Cardiac Bioengineering and Professor of Surgery with Boston Children's Hospital, Harvard Medical School, Boston, MA, USA where his group develops instrumentation and imaging technology for minimally invasive surgery.